Eur. J. Mineral., 37, 639–666, 2025
https://doi.org/10.5194/ejm-37-639-2025

European Journal of Mineralogy
Open Access

Origin and evolution of the Variscan Léon eclogites: insights from zircon and garnet petrochronology

Lorraine Tual[1], Christine Authemayou[1], Caroline Lotout[2,3], Matthijs A. Smit[4,5], Kira Musiyachenko[4], Denise Bussien Grosjean[6], Ellen Kooijman[5], and Emilie Bruand[1]

[1]Geo-Ocean, Univ. Brest, CNRS, Ifremer UMR6538, 29280 Plouzané, France
[2]Laboratoire Magmas et Volcans, Université Clermont Auvergne, CNRS, IRD, OPGC, 63000 Clermont-Ferrand, France
[3]Centre de Recherche Pétrologiques et Géochimiques, Université de Lorraine, CNRS, 54000 Nancy, France
[4]Department of Earth, Ocean & Atmospheric Sciences, University of British Columbia, Vancouver V6T 1Z4, Canada
[5]Department of Geosciences, Swedish Museum of Natural History, 104 05 Stockholm, Sweden
[6]Direction de L'environnement Industriel, Urbain Et Rural, Direction Générale de L'environnement, Etat de Vaud, Chemin Des Boveresses 155, 1066 Épalinges, Switzerland

Correspondence: Lorraine Tual (lorraine.tual@univ-brest.fr)

Received: 10 January 2025 – Revised: 2 July 2025 – Accepted: 4 July 2025 – Published: 1 October 2025

Abstract. Eclogites record the deep burial and exhumation of crustal terranes, which are key tectonic markers in the evolution of orogenic belts. Unraveling the evolution of eclogites and eclogite-bearing terranes may nevertheless be challenging, especially in old and poly-tectonic orogens such as the Variscan orogen, where these are scarce and potentially reworked. The eclogite-bearing Léon Domain (Armorican Massif, France) is one such occurrence. The Léon Domain is situated at the crossing of several (micro)continents and has long been recognized as a potential recorder for the assembly of this part of the Variscan orogen. The origin and metamorphic history of these eclogites remains nevertheless largely unconstrained. In this study, samples of the Léon eclogite were subjected to garnet and zircon petrochronology. In situ U-Pb ages from zircon cores constrain the protolith age at 385.7 ± 2.9 Ma (concordia age, mean square weighted deviate (MSWD) = 8.7 and corresponding weighted mean age at 385.7 ± 1.6 Ma, MSWD = 1.14), which is similar to zircon U-Pb ages reported from enclosing orthogneisses. Low $\delta^{18}O$ values (median at 4.32 ‰) from these cores indicate interaction with surface fluids during magmatic crystallization. Garnet growth in the eclogites, as constrained by Lu-Hf geochronology, occurred at 346.5 ± 0.8 Ma (MSWD = 0.6; Fe-Ti-rich eclogite) and 349.1 ± 1.6 Ma (MSWD = 0.3; kyanite-bearing eclogite). Pseudosection modeling, Zr-in-rutile thermometry, and major- and trace-element maps in garnet were used to constrain the garnet growth history close to the metamorphic peak from 740 °C at 2.15 GPa to 760 °C at 2.5 GPa. Zircon separates from a cross-cutting felsic intrusion provided 321.6 ± 2.7 Ma (MSWD = 0.76), which is taken to constrain the age of deformation and migmatization during exhumation. The new results are inconsistent with the presence of a major suture in the Léon Domain; they instead indicate that the eclogite derives from a small and short-lived back-arc basin, in which large bodies of felsic magma (enclosing orthogneiss) and smaller basaltic intrusions (the eclogite protolith) were emplaced and allowed to interact with meteoric water. The Léon Domain records rapid, cyclic inversion of this basin and thus may serve as an ancient analogue to the evolution of the Central Neotethys system, where short-lived alternating pulses of crustal extension and compression correlate with episodes of trench retreat and advance. The new tectonic interpretation for the Léon Domain supports a strong control of the slab dynamics within the frame of the protracted subduction history of the Rheic paleo-ocean.

1 Introduction

Remnants of deeply eroded mountain belts may contain high-pressure (HP) rocks, which may preserve a record of the early subduction and collision processes that occurred when the orogenic system started to develop (e.g., Coleman et al., 1965; Maruyama et al., 1996; Godard, 2001; Agard et al., 2009; Johnson and Harley, 2012; Zheng, 2012; Warren, 2013; Kohn, 2014; Tual et al., 2017; Tsujimori and Mattinson, 2021; Lotout et al., 2023). The protolith of these rocks can also provide key insight into provenance and the pre-orogenic setting of a region (Rubatto, 2002; Kylander-Clark et al., 2012; Gilotti, 2013; Kooijman et al., 2017; Engi, 2017; Lotout et al., 2020; Tual et al., 2022b). Strong metamorphic overprinting and tectonic reworking of HP rocks, however, makes unraveling their pressure–temperature–time (P–T–t) paths far from trivial (e.g., Spear, 1993). Zircon and garnet provide opportunities to look far back into the history of these rocks. Zircon can provide chronological, elemental and isotopic constraints on the protolith and various stages of subduction (e.g., Kohn et al., 2015; Rubatto, 2017). One specific advantage of zircon over most chronometers is that it may crystallize in both igneous and metamorphic rocks and, due to its robustness, may preserve a unique archive of the protolith even in high-grade metamorphic rocks (e.g., Petersson and Tual, 2020). Combined with O stable isotope analyses, zircon petrochronology is particularly relevant to investigate the paleo-setting and origin of the protolith magma; rocks and fluid sources show a limited range of δ^{18}O values, and no significant T-dependent shifts in δ^{18}O values of most minerals occur in closed systems (e.g., Bebout and Barton, 1989; Sharp et al., 1993; Barnicoat and Cartwright, 1997; Putlitz et al., 2000; Scambelluri et al., 2004; Angiboust et al., 2014; He et al., 2019; Vho et al., 2020; Bovay et al., 2021). The greatest challenge of zircon petrochronology is linking U-Pb age data from zircon to petrogenetic processes and their P–T conditions. Zircon can (re)crystallize over a wide range of conditions in rocks, causing superimposition of numerous processes that may be difficult to disentangle (e.g., Rubatto, 2017). Retrieving the timing of HP conditions is highly sample-dependent and particularly challenging in mafic rocks, where zircon grains are typically small (< 100 µm; e.g., Beckman et al., 2014). Garnet petrochronology has several advantages that make it a strong complementary approach in investigating early stages of metamorphic histories. Used in conjunction with pseudosection modeling, garnet can provide a comprehensive record of the deep burial of HP rocks and the tectonic and geodynamic processes that this burial may represent (e.g., Kylander-Clark et al., 2007; Pollington and Baxter, 2010; Smit et al., 2010; Dragovic et al., 2015; Cutts and Smit, 2018; Loury et al., 2018; Lotout et al., 2018; Tual et al., 2022a, 2025). Garnet enables the reconstruction of the P–T–t evolution experienced by HP rocks through a combination of petrologic, major- and trace-element analysis and geochronology. Recent analytic improvements on trace-element (TE) mapping in garnet (e.g., Woodhead et al., 2007; Paul et al., 2014) have revolutionized garnet-based metamorphic geology. Trace elements such as Cr, Ti and rare earth elements (REEs) exhibit greater resilience to diffusional re-equilibration than major elements and are overall more sensitive to the subtle geochemical changes that occur during metamorphic reactions (e.g., Raimondo et al., 2017; George et al., 2018; Rubatto et al., 2020; Tual et al., 2022a; Konrad-Schmolke et al., 2023; Kulhánek and Faryad, 2023; Cruciani et al., 2024). Additionally, garnet typically has high Sm/Nd and Lu/Hf values, enabling dating using the ^{147}Sm-^{143}Nd and ^{176}Lu-^{176}Hf chronometers (Griffin and Brueckner, 1980; Duchêne et al., 1997). Garnet Lu-Hf chronology is among the most robust mineral chronometers available: even grains smaller than 1 mm may perfectly retain age information during extreme metamorphic cycles lasting for hundreds of millions of years and involving (ultra)high T (Scherer et al., 2000; Smit et al., 2013; Baxter and Scherer, 2013; Cutts et al., 2019; Tual et al., 2022b; Lotout et al., 2023). In this study, both zircon and garnet petrochronology have been employed to investigate the so-far enigmatic history of the Variscan Léon eclogites.

The Léon Domain is situated at the westernmost tip of Brittany in the Armorican Massif and part of the Variscan Orogen of Europe – one of the most populated orogenic belts in the world. The domain represents a window into several (micro)continents – Armorica, Avalonia and Gondwana – which collided as part of the Variscan orogeny (e.g., Matte, 1986; Murphy et al., 2009; Ballèvre et al., 2009; Kroner and Romer, 2013; Franke et al., 2021; Ballèvre et al., 2014). The Léon Domain constitutes most of the northwestern part of the Armorican Massif in the region, and its geodynamic affiliation and evolution is a long-standing debate, due to the presence of a still largely uncharacterized eclogite occurrence. The Léon Domain is either considered a distinct crustal block, i.e., the Normanian Terrane (Nutman et al., 2023), or as a part of the Armorican Terrane Assemblage (Shail and Leveridge, 2009) that correlates laterally with the Saxo-Thuringian zone in Bohemia to the east (e.g., Ballèvre et al., 2009; Schulmann et al., 2022, 2023) and the Finistera block in Iberia to the southwest (Mateus et al., 2016; Moreira et al., 2019). The Léon Domain is separated from Armorica by a major fault (the Elorn structure) or a suture zone (Le Conquet suture; Rolet et al., 1986; Faure et al., 2005, 2010), although these interpretations have been contested by some authors (e.g., Schulz et al., 2007) on the basis of the geodynamic models proposed by Rolet et al. (1986) and Faure et al. (2005), being rooted in qualitative interpretations. First-order information on metamorphism and chronology, as well as detailed field-based observations, is lacking in large parts of the Léon Domain, preventing the establishment of a robust geodynamic model for the region. Despite limited exposure and detailed datasets, two major characteristics can be drawn: (1) no deformation gradient, inverted metamor-

phic gradient or metamorphic gaps have been documented near the proposed nappe boundaries, which are prerequisites for the nappe tectonics interpretation (Schulz et al., 2007; Le Gall et al., 2014); (2) available chronological data are patchy and incomplete, relying on imprecise and possibly inaccurate data from accessory phases (e.g., see Paquette et al., 1995, 2017, for a critical review of ages proposed by Paquette et al., 1987).

Considering the Léon Domain as an "exotic" block with respect to the rest of the Armorican Massif (e.g., Nutman et al., 2023) is inspired by its apparent higher P–T record of Variscan metamorphism. The eclogite-facies conditions and partial migmatization reflected in this domain contrast with the surrounding Northern Armorican and Central Armorican domains, which show little or no HP metamorphism. Constraints on the history of the HP rocks of the Léon Domain clearly is of pivotal importance in resolving the tectonic history of the region, determining the spatial and temporal imprint of the Variscan orogeny in the Armorican massif, and making correlations at the orogen scale. To obtain these constraints, precise age data associated with the origin and evolution of the eclogites of the Léon eclogites and a robust quantification of the peak metamorphic conditions are required. In this contribution, we combined garnet and zircon petrochronology in two eclogite samples of different compositions from a single mafic lens in the Léon Domain located in Plounévez-Lochrist: (1) a remarkably well-preserved kyanite-bearing eclogite and (2) a Fe-Ti-rich, partly retrogressed eclogite. To constrain the final deformation and anatexis stages, we also analyzed a granitic intrusion from the same unit that formed from the partial melting, concurrent with the exhumation of the Léon Domain during its exhumation. Together, the new data better constrain the HP and final high-temperature (HT) metamorphic events in the region and enable the proposition of a geodynamic model for the Léon Domain and its role in the Variscan orogeny.

2 Geological context and sampled lithologies

The Variscan orogenic belt is a largely eroded collisional zone resulting from the Early Carboniferous (360–340 Ma) closure of variably developed oceanic basins and the subsequent collision of large continental plates (Avalonia/Laurussia and Gondwana) with Gondwana-derived, ribbon-like microcontinents (e.g., Matte, 1986, 2001; Tait, 1999; Ballèvre et al., 2009; Stampfli et al., 2013; Franke et al., 2017, 2021; Fig. 1a). The Rheic Ocean, which separated Gondwana and Laurussia (e.g., Ballèvre et al., 2009), was central to this geodynamic setting. The lateral extent and general paleogeographic setting nevertheless are still unclear (e.g., Schulmann et al., 2022). The location of the main and secondary sutures remains difficult to ascertain, because the Rheic Ocean – much like the Tethyan and Neotethyan – likely involved complex multistage closure (e.g., Stampfli et al., 2002; Alexander et al., 2019), yet its relics are far less well exposed. Armorica, which is one of the Gondwana-derived microcontinents, is exposed in the Armorican Massif in the NW segment of the Variscan orogenic belt (Fig. 1a; Servais and Sintubin, 2009; Stampfli et al., 2013, and references therein). The Armorican Massif consists of four structural domains – the North Armorican, Central Armorican, South Armorican domains (NAD, CAD and SAD) and the Léon Domain to the northwest – which were tectonically juxtaposed along the dextral North Armorican and South Armorican shear zones (Fig. 1a, b; NASZ: North Armorican Shear Zone; PGSZ: Porspoder-Guissény Shear Zone; Gapais and Le Corre, 1980; Le Corre et al., 1991).

The Armorican Massif is bounded to the north by a suture with the Lizard Complex in Cornwall (England) and to the southwest by the Iberian units. The tectonic boundaries are hidden by the English Channel (La Manche) and the Bay of Biscay, which formed during a Mesozoic rifting phase (e.g., Ziegler, 1987, 1994). The Lizard Complex was traditionally thought to mark the main suture of the Rheic Ocean – a view that has been repeatedly challenged (e.g., Floyd, 1984; Cook et al., 2002; Leveridge and Shail, 2011; Alexander et al., 2019), most recently by a geochronological study that instead suggests the Lizard Complex to represent a short-lived rift, inverted shortly after 400 Ma, while a subduction continued southwards (Nutman et al., 2023). This interpretation implies that the final suture of the Rheic Ocean must be located further south, beneath today's English Channel. Close paleogeographical connections and a shared Cadomian orogenic signature correlate the Armorican domains with Iberian units (Young, 1990; Ballèvre et al., 2009; Ribeiro et al., 2009; Franke, 2014; Franke et al., 2017; Fig. 1a). Together, these zones form the Ibero-Armorican Arc, of which the Cantabrian Orocline is interpreted as a secondary structure formed by buckling during the late orogenic phase (310–295 Ma; e.g., Pastor-Galán et al., 2015; Weil et al., 2001, 2013; Martínez Catalán et al., 2024). Within the arc, the activation of major transcurrent fault systems facilitated lateral mass transfer, amplifying the orogenic structure (Arthaud and Matte, 1977; Burg et al., 1994; Gapais et al., 2015; Gutiérrez-Alonso et al., 2012; Matte and Ribeiro, 1975; Martínez Catalán, 2011).

The Léon Domain in the northwestern part of the Armorican massif is exposed in a $30 \times 80\,km^2$ metamorphic dome structure characterized by two cores along a N70° E-trending axial zone (Tréglonou and Plounévez-Lochrist orthogneisses, Fig. 1b; Paquette et al., 1987; Le Gall et al., 2014; Authemayou et al., 2019). The dome is intersected to the north, center and south by E–W- to NE–SW-striking ductile transcurrent shear zones. Three major phases of Variscan deformation have been documented: (1) northeast-directed transpressive crustal shearing before 340 Ma; followed by (2) transtensive deformation associated with SW-directed shearing on S-dipping foliation and partitioned with E–W-directed dextral shearing zones contemporaneously with in-

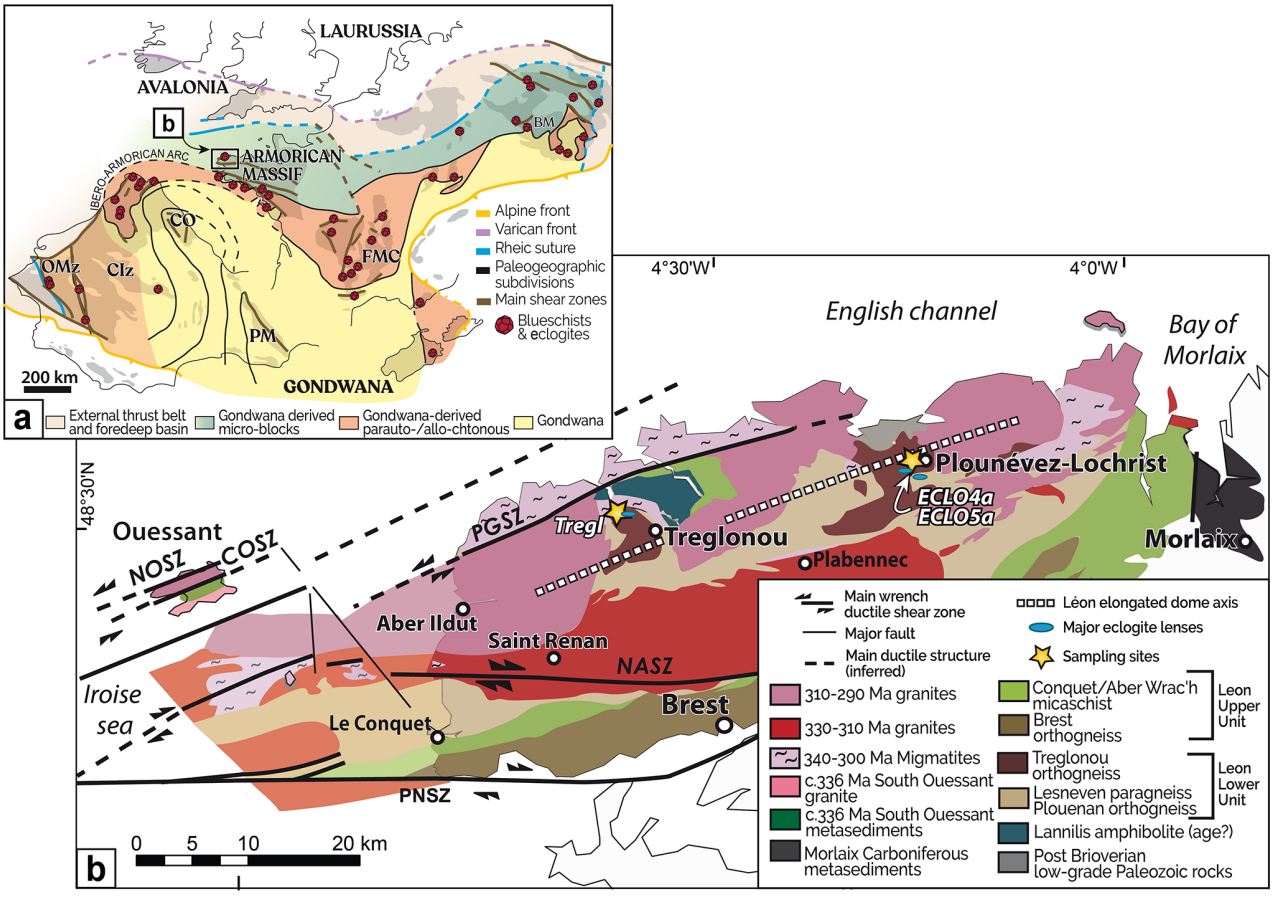

Figure 1. Geological context of the Léon Domain. **(a)** Structural map and main tectonostratigraphic units of the European Variscan belt. Modified from Authemayou et al. (2019), adapted from Martínez Catalán (2011) and Franke et al. (2021). NASZ: North Armorican Shear Zone; PNSZ: Pierres Noires Shear Zone/Élorn; PGSZ: Porspoder-Guissény Shear Zone ; NASZ: North Armorican Shear Zone; NOSZ: North Ouessant Shear Zone; COSZ: Central Ouessant Shear Zone; BM: Bohemian Massif; CIz: Central Iberian zone; FMC: French Massif Central; PM: Pyrenean Massif; CO: Cantabrian Orocline; OMz: Ossa Morena zone. **(b)** Léon Domain showing the main lithologies and structural units, shear zone patterns, Tournaisian-Visean basins and the two sampling sites.

trusive complexes between 330 and 310 Ma (Balé and Brun, 1986; Rolet et al., 1986; Faure et al., 2010; Schulz, 2013; Le Gall et al., 2014; Authemayou et al., 2019); and (3) late deformation restricted to the north of the Léon Domain, with sinistral WSW–ESE shearing (Porspoder-Guissény Shear Zone) with the emplacement of syn-kinematic granitoids at 300 Ma (Caroff et al., 2015).

The metamorphic evolution of the Léon Domain is largely based on major-element chemistry of mineral assemblages with generally limited robust geochronological constraints (Cabanis and Godard, 1987; Chantraine et al., 1986; Godard and Mabit, 1998; Jones, 1993, 1994; Paquette et al., 1987; Schulz, 2013; Schulz et al., 2007). Two main units are broadly defined based on their metamorphic sequences: the Upper Unit corresponds to amphibolite-facies Conquet-Penze Micaschist Unit and the Lower Unit corresponds to overall higher-grade lithologies including the Lesneven Gneiss Unit (Fig. 1b; Balé and Brun, 1986; Cabanis et al., 1977, 1979; Cabanis and Godard, 1987; Le Corre et al., 1989, 1991; Rolet et al., 1986; Rolet, 1994; Faure et al., 2010). These two metamorphic units are not separated by major tectonic contacts, and there is no evidence for thrust tectonics in the Léon that would juxtapose HP over low-pressure (LP) nappes (Schulz et al., 2007). The Upper Unit situated in the southern section of the dome followed a clockwise P–T path from 0.5 Ga at to 0.8 GPa at 600 °C and underwent heating during decompression; the degree of metamorphism increases overall towards the northwest from greenschist-facies to supra-solidus conditions (Jones, 1994; Schulz et al., 2007; Faure et al., 2010; Schulz, 2013). In the Lower Unit, mafic lenses record eclogite-facies conditions, with peak P–T conditions estimated to have been at least 1.3–1.4 GPa at 650–700 °C (Cabanis and Godard, 1987; Paquette et al., 1987; Godard and Mabit, 1998). The HP metamorphism was tentatively dated at 439 ± 12 Ma (Paquette et al., 1987). However, the method used – ". isotope-dissolution thermal ion-

ization mass spectrometry (ID-TIMS) U-Pb dating of multigrain zircon – makes reliable geological interpretation of this age difficult (e.g., Paquette et al., 1995, 2017). The Lower Unit underwent decompression and cooling from granulite to amphibolite facies (from 0.8 GPa at 800 °C to 0.5 GPa at 500 °C), culminating in LP migmatization (0.5–0.4 GPa at 600–500 °C; Cabanis and Godard, 1987; Chantraine et al., 1986; Godard and Mabit, 1998; Paquette et al., 1987; Schulz et al., 2007). Weighted-mean U-Th-Pb ages from in situ analysis of monazite in the Plounévez-Lochrist orthogneiss, Lesneven gneiss and Conquet micaschist range between 340 and 300 Ma, with a main peak at ca. 315 Ma (Schulz, 2013). The latter age is concomitant with the age of emplacement of the syn-tectonic Saint-Renan granite and Groac'h Zu intrusive complex (316 ± 2 Ma; 318 ± 2 Ma, respectively; laser ablation inductively coupled plasma mass spectrometry (LA-ICPMS) U-Pb on zircon by Le Gall et al., 2014) along the dextral North Armorican Shear Zone and the Pierres Noires Shear Zone. These events were followed by the intrusion of the Aber Ildut-Brignogan granite (303.8 ± 0.9 Ma; LA-ICPMS U-Pb on zircon; Caroff et al., 2015) along the sinistral N50° E Porspoder-Guissény Shear Zone.

Retrogressed former eclogitic rocks occur in a dozen relatively small tectonic lenses (< 1 km long) between the localities of Plouider and Plounévez-Lochrist and locally near Tréglonou (Fig. 1b; e.g., Lacroix, 1889, 1891; Guffroy, 1958; Cabanis and Godard, 1987; Paquette et al., 1987). The eclogite-bearing lenses occur mostly along the boundary of (and within) the Tréglonou and Plounévez-Lochrist orthogneisses and the Lesneven paragneiss, with a few lenses also documented in the Plouénan monzogranitic orthogneiss. All these lithologies belong to the Lower Unit of the Léon Domain. The Tréglonou and Plounévez-Lochrist orthogneisses belong to the same complex, and their protolith crystallization age was dated at ca. 390 Ma (ID-TIMS U-Pb zircon; Marcoux et al., 2009). The Lesneven paragneiss is a biotite, sillimanite-bearing micaschist, which yielded ages of 514 ± 16 Ma and 527 ± 11 Ma (U-Th-Pb, in situ electron probe microanalyzer (EPMA) on monazite; Schulz, 2013) and 581 ± 36 Ma (U-Th-Pb, in situ EPMA on a single monazite core; Marcoux et al., 2009); the age of Plouénan orthogneiss is unknown.

Three major types of eclogites were recognized (Lacroix, 1889, 1891; Cabanis and Godard, 1987; Godard and Mabit, 1998), comprising a kyanite-bearing, a quartz-rich and a Fe-Ti-rich variety. Constraints on the protolith and geodynamic origin of the eclogites are limited, but major-element and trace-element chemistries are compatible with gabbroic rocks (kyanite-bearing type) and associated restitic melt (Fe-Ti type) of N-MORB basaltic rock derived from partial melting of a mantle source (Cabanis and Godard, 1987; Paquette et al., 1987). Radiogenic Nd isotope compositions indicate a juvenile source with insignificant crustal contamination (Paquette et al., 1987). All the eclogite occurrences reflect extensive overprinting during widespread heating and decompression (Godard and Mabit, 1998); pristine omphacite in the matrix of these rocks has been entirely replaced by diopside (± amphibole) and plagioclase symplectites.

Two eclogite varieties were sampled in this study. Samples were taken out of a blasted outcrop from the same Kerscao (900 × 250 m) lens in Plounévez-Lochrist (48°36′34.3″ N, 4°13′09.9″ W): sample *ECLO5a* represents a Fe-Ti-rich eclogitic layer (Fig. 2a), whereas sample *ECLO4a* is an exceptionally well-preserved kyanite-bearing eclogite (Fig. 2b, c). A third sample *Tregl* was taken from an orthogneiss outcrop at Treglonou (48°33′16.21″ N, 4°34′28.9″ W), situated in the same unit as the Plounévez-Lochrist orthogneiss and along the northern flank of the western core of the migmatite dome in which eclogites were exhumed (all samples indicated with a star in Fig. 1b). The sample represents a granitic intrusion with a dominant pervasive foliation (S1) defined by the preferred orientation of quartz, feldspar and biotite (Fig. 2d). This planar fabric is oriented dominantly N100° E, dipping 45 to 70° to the north, and carries a pervasive stretching lineation that plunges on average 50° towards N to NE (Fig. 2d). The schistosity is closely associated with north-dipping shear planes (C1), in pervasive S-C fabrics, indicating a top to the north shearing. The two planes are overprinted by a younger ductile deformation corresponding to SE-dipping extensional shear zones (C2). Magmatic intrusions fill these extensional shear zones (Fig. 2d). The diffuse boundary between the planar intrusions and the orthogneiss, with some magma injections along the orthogneiss schistosity indicates syn-extensional magmatic emplacement on these shear zones. The sample therefore corresponds to an intrusion in an extensional shear zone (Fig. 2d), which records late melting during exhumation of the core complex.

3 Methods

3.1 Mineral analysis and major-element X-ray maps

Mineral spot analyses and X-ray element maps were performed using a CAMECA SX-100 EPMA at the Pôle Spectrométrie Océan, Ifremer, Plouzané, France. Spot analyses (1 µm or defocused to 5 µm for amphibole, mica and chlorite) were done at 15 kV, 20 nA and 10 s on-peak counting time, except for Ti (30 s). The following natural standards were used: wollastonite (Si, Ca), corundum (Al), andradite (Fe), forsterite (Mg), $MnTiO_3$ (Mn, Ti), albite (Na), orthoclase (K), apatite (P) and Cr_2O_3 (Cr). Estimation of Fe^{3+} concentrations in Table 1 was done using the software AX_6.2 (Holland, 2018), and structural formulae were calculated based on 8 cations for garnet, 11 oxygens for mica, 8 oxygens for feldspar and 23 oxygens for amphibole. Representative mineral compositions are presented in Table 1 and Fig. 3 and plotted using MinPlot software (Walters, 2022). End-members are defined as mole fractions: for garnet $X_{Grs} = Ca/(Ca+Fe+Mn+Mg)$; $X_{Prp} = Mg/(Ca+Fe+Mn+Mg)$; $X_{Sps} = (Mn/Ca+Fe+Mn+Mg)$; $X_{Alm} = Fe^{2+}/(Ca+Fe+$

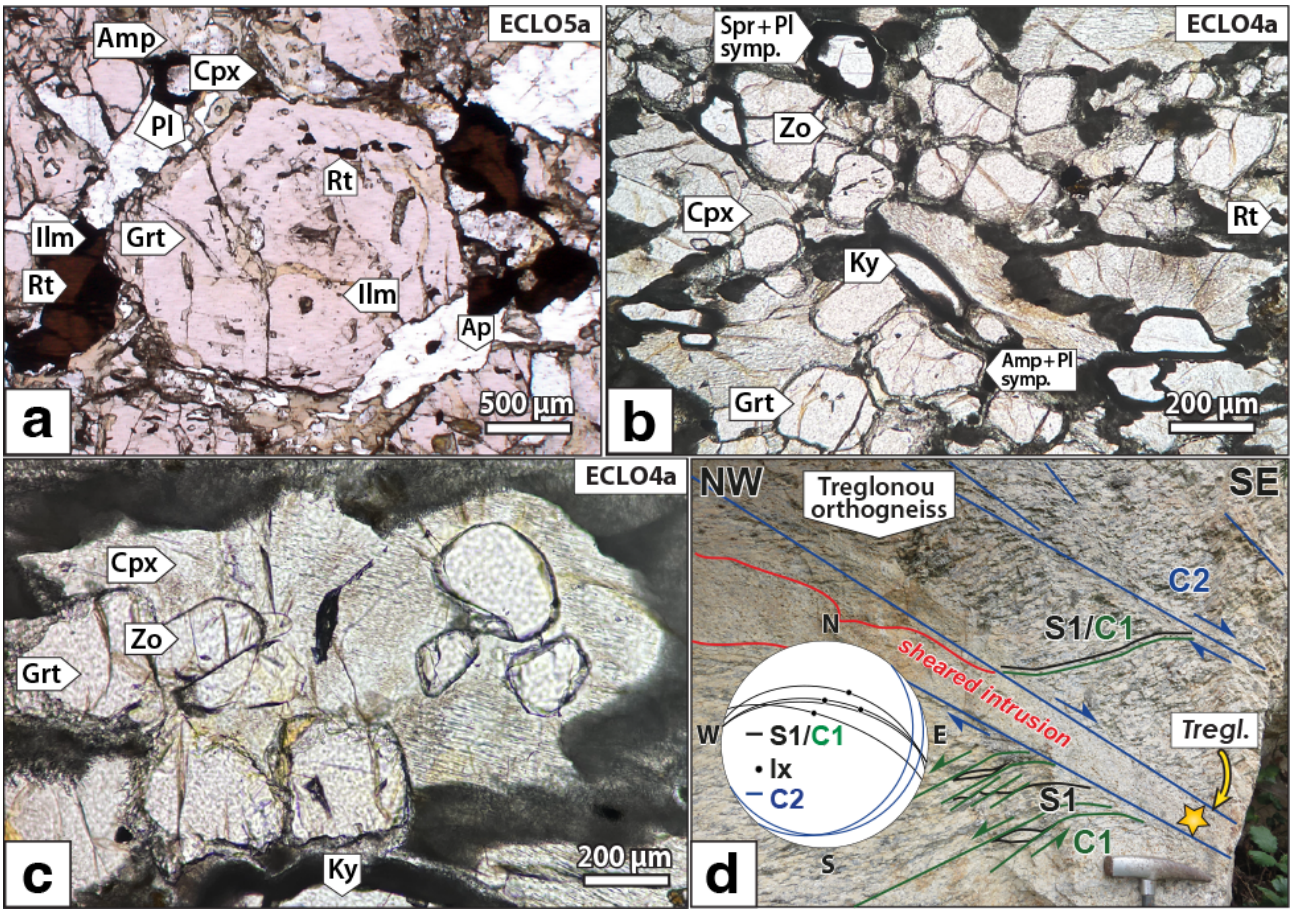

Figure 2. Photographs of the selected samples showing **(a)** a retrogressed Fe-Ti-rich eclogite (*ECLO5a*), **(b)** the main high-pressure paragenesis partly replaced by symplectites in the kyanite-bearing eclogite sample (*ECLO4a*), **(c)** a large omphacitic clinopyroxene enclosing garnet and zoisite (*ECLO4a*) and **(d)** the sheared intrusion sample ("*Tregl*" represented with a yellow star) located in a crosscutting migmatitic vein; the major structural characteristics (planar: S1, C1, C2; linear: lx) are outlined in the stereogram and in the photograph.

Mn + Mg) and for omphacite, X_{Jd} follows Morimoto (1988). Major-element X-ray mapping was done at 15 kV, 40 nA, a dwell time per step of 400 ms, and a step size of ca. 3 µm over a mapping area of 6 × 7 mm (*ECLO5a*) or 1.6 × 2.6 mm (*ECLO4a*). Post-processing was done using XMapTools 4.3, build 240114 (Lanari et al., 2014, 2019). Quantitative maps were calculated from 262 (*ECLO4a*) and 147 (*ECLO5a*) data points obtained from spot analyses and profiles on the map area. Representative quantitative maps are presented in Fig. 4.

3.2 Zr-in-rutile thermometry and pseudosection modeling

Zirconium concentrations in rutile were measured on *ECLO4a* thin sections (along with Cr, Fe, Nb, Si and V to monitor potential contributions of micro-inclusions) using the same EPMA. A zircon metal SP005 was used as primary standard. Analyses of Zr k_α on pentaerythritol (PET) were performed at 25 kV and 150 nA for 100 s. Spot analyses were performed with a diameter of 1 µm. Detection limits were consistently ca. 80 ppm. Zirconium-in-rutile calculations were performed with an estimated a_{ZrSiO_4} of 1, as zircon is found in the cores of garnet as well as in the matrix of *ECLO4a*; a_{SiO_2} is estimated to be 1 for garnet core inclusions as quartz is present. For rutile in garnet rims and matrix rutile, where quartz is not observed, Zr-in-rutile provides *maximum T* estimates, as a_{SiO_2} may have been less than unity. Thermometric results obtained using the calibration of Tomkins et al. (2007) are provided in Table S4 in the Supplement.

Pseudosections were performed using local bulk compositions of the quantitative maps obtained for the *ECLO4a* sample (Fig. 5; from domain area presented in Fig. 3f), using XMapTools 4.3. Sulfide-rich minerals were excluded from the bulk composition based on calculations from the quantified phase map (Fig. 3f; Tual et al., 2017). Pseudosections were calculated using Theriak-Domino (de Capitani and Brown, 1987; de Capitani and Petrakakis, 2010), using the Holland and Powell (2011) internally consistent thermodynamic dataset (ds6.2; updated in White et al.,

Table 1. Representative mineral analyses.

Sample	ECLO4a pf3_53	ECLO4a pfg4_18	ECLO4a pf3_7	ECLO4a pfo3_31	ECLO4a pfo3_93	ECLO4a pfa1_42	ECLO4a 4a2_74	ECLO4a pfe1_32	ECLO5a pf1-26	ECLO5a pf1-36	ECLO5a pf1-5	ECLO5a x-15	ECLO5a 2-49	ECLO5a x-11	ECLO5a x-23	ECLO5a x-29
Mineral	Grt	Grt	Grt	Cpx	Cpx	Amp	Amp	Zo	Grt	Grt	Grt	Cpx	Amp	Amp	Pl	Or
Location	core	mantle	rim	core	rim	i. Cpx	symp	matrix	core	mantle	rim	symp	i. Grt	symp	symp	symp
avPT		*x*		*x*		*x*		*x*								
SiO_2	39.47	39.98	39.25	56.86	54.99	49.80	45.00	39.34	37.45	37.32	38.66	52.70	40.66	44.66	65.17	65.15
TiO_2	0.06	0.00	0.04	0.11	0.19	0.42	0.14	0.09	0.03	0.04	0.01	0.18	0.59	0.69	0.00	0.00
Al_2O_3	22.52	22.70	22.42	10.67	9.72	11.73	13.75	31.89	20.60	20.98	21.73	3.26	18.21	12.78	21.96	18.30
Cr_2O_3	0.00	0.00	0.08	0.05	0.03	0.02	0.07	0.07	0.00	0.00	0.00	0.00	0.00	0.00	0.00	0.00
Fe_2O_3*	2.20	1.54	2.03	0.00	0.00	1.54	4.88	1.84	1.41	2.19	1.88	0.33	4.31	2.63	0.08	0.33
FeO	16.80	16.25	18.19	2.54	2.97	3.92	4.49	0.02	27.44	27.40	23.25	7.68	10.97	11.60	0.00	0.00
MnO	0.47	0.40	0.54	0.00	0.00	0.00	0.08	0.00	4.48	2.92	0.47	0.15	0.13	0.11	0.00	0.00
MgO	10.24	11.03	10.55	9.04	10.94	17.22	15.92	0.13	2.21	1.81	7.39	12.94	10.20	12.03	0.02	0.01
CaO	9.15	8.97	7.36	14.63	17.28	10.57	10.19	23.90	6.90	8.39	7.22	22.01	10.41	11.75	3.16	0.00
Na_2O	0.00	0.00	0.00	5.52	4.51	2.92	3.03	0.00	0.01	0.07	0.02	0.88	2.26	1.94	10.26	0.09
K_2O	0.00	0.00	0.00	0.00	0.00	0.00	0.00	0.00	0.00	0.00	0.00	0.00	0.38	0.09	0.07	16.08
Totals	100.91	100.87	100.46	99.42	100.63	98.14	97.55	97.27	100.53	101.12	100.63	100.13	98.12	98.28	100.72	99.96
Oxygens	12.00	12.00	12.00	6.00	6.00	23.00	23.00	12.50	12.00	12.00	12.00	6.00	23.00	23.00	8.00	8.00
Si	2.95	2.97	2.95	2.01	1.95	6.91	6.41	3.01	2.99	2.96	2.96	1.95	5.94	6.49	2.854	3.01
Ti	0.00	0.00	0.00	0.00	0.01	0.04	0.02	0.01	0.00	0.00	0.00	0.01	0.07	0.08	0.00	0.00
Al	1.98	1.98	1.98	0.45	0.41	1.92	2.31	2.88	1.94	1.96	1.96	0.14	3.14	2.19	1.13	1.00
Cr	0.00	0.00	0.01	0.00	0.00	0.00	0.01	0.00	0.00	0.00	0.00	0.00	0.00	0.00	0.00	0.00
Fe^{3+}	0.12	0.09	0.12	0.00	0.00	0.16	0.52	0.11	0.08	0.13	0.11	0.01	0.48	0.29	0.00	0.01
Fe^{2+}	1.05	1.01	1.14	0.08	0.09	0.46	0.54	0.00	1.83	1.82	1.49	0.24	1.34	1.41	0.00	0.00
Mn	0.03	0.03	0.03	0.00	0.00	0.00	0.01	0.00	0.30	0.20	0.03	0.01	0.02	0.01	0.00	0.00
Mg	1.14	1.22	1.18	0.48	0.58	3.56	3.38	0.02	0.26	0.21	0.85	0.71	2.22	2.61	0.00	0.00
Ca	0.73	0.71	0.59	0.56	0.66	1.57	1.56	1.96	0.59	0.71	0.59	0.87	1.63	1.83	0.15	0.00
Na	0.00	0.00	0.00	0.38	0.31	0.79	0.84	0.00	0.00	0.01	0.00	0.06	0.64	0.55	0.87	0.01
K	0.00	0.00	0.00	0.00	0.00	0.00	0.00	0.00	0.00	0.00	0.00	0.00	0.07	0.02	0.00	0.95
Sum	8.00	8.00	8.00	3.95	4.00	15.40	15.58	7.99	8.00	8.00	8.00	4.00	15.54	15.47	5.02	4.97
X_{Grs}	0.25	0.24	0.20	X_{Jd} 0.36	X_{Jd} 0.30				0.20	0.24	0.20	X_{Jd} 0.06				
X_{Prp}	0.39	0.41	0.40						0.09	0.07	0.29					
X_{Sps}	0.01	0.01	0.01						0.10	0.07	0.01					

* estimated from stoichiometry. $X_{Grs} = Ca/(Ca + Mg + Mn + Fe)$; $X_{Prp} = Mg/(Ca + Mg + Mn + Fe)$; $X_{Sps} = Mn/(Ca + Mg + Mn + Fe)$, X_{Jd} after Morimoto (1988). Grt: garnet; Cpx: Clinopyroxene; Amp: Amphibole; Zo: zoisite: Or: orthoclase; Pl: plagioclase.

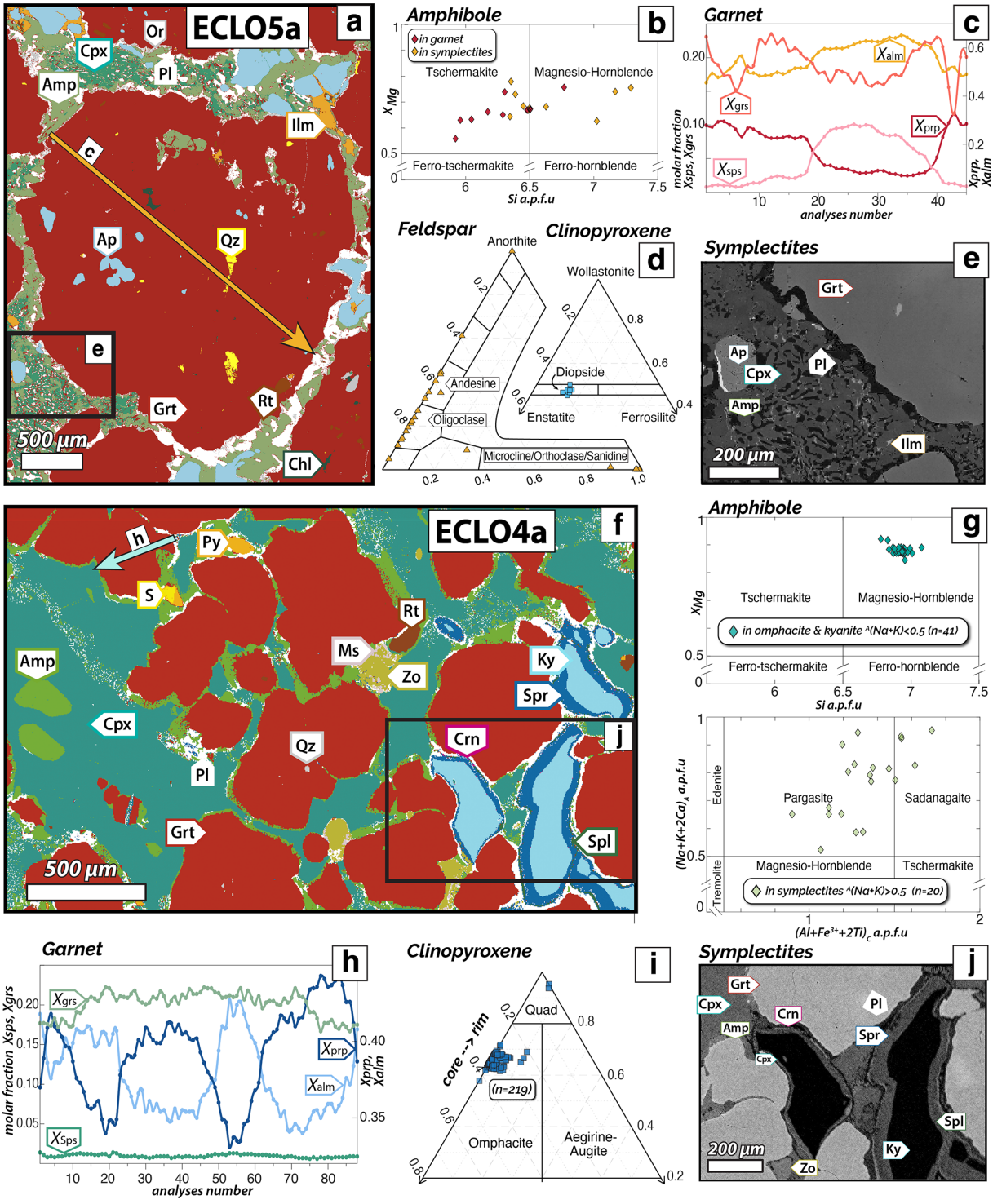

Figure 3. Petro-chemical characteristics of the eclogite samples *ECLO5a* **(a–e)** and *ECLO4a* **(f–j)**. **(a)** Mineral map of the partly retrogressed Fe-Ti-rich sample; **(b)** composition of amphibole included in garnet and in clinopyroxene symplectites; **(c)** garnet compositional profile across the grain in **(a)**; **(d)** composition of feldspar from garnet coronas and former high-pressure clinopyroxene symplectites and retrogressed clinopyroxene compositions; **(e)** close-up from **(a)** showing former high-pressure symplectites now replaced by amphibole, exsolved plagioclase and diopside. **(f)** mineral map of the partly retrogressed kyanite-bearing sample; **(g)** composition of amphibole included in clinopyroxene and kyanite and in garnet symplectites; **(h)** garnet compositional profile across the grain in **(f)**; **(i)** composition of high-pressure clinopyroxene; **(j)** close-up from **(f)** showing micrometer-scale symplectite coronas around kyanite.

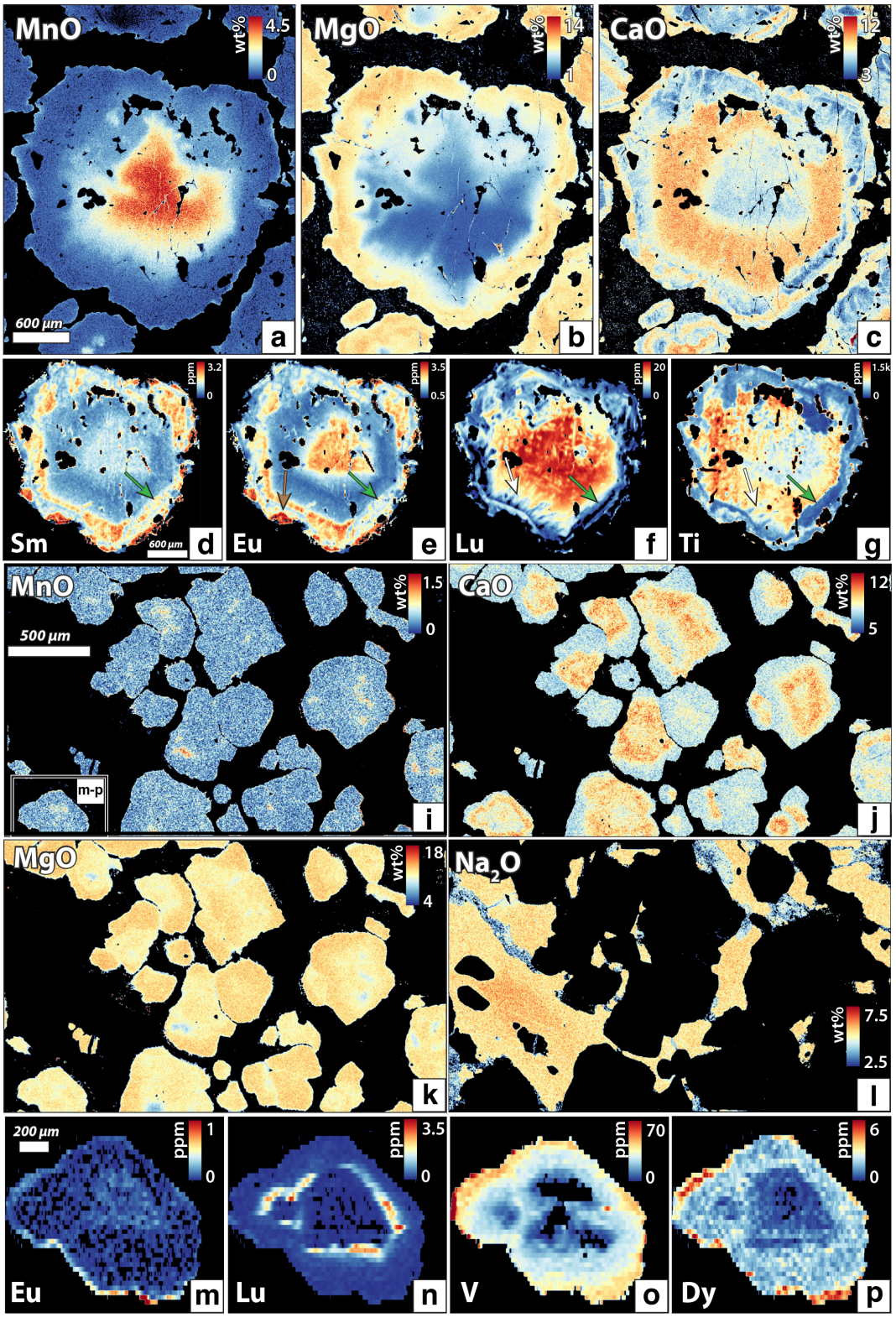

Figure 4. Major- and trace-element quantitative maps of the eclogite samples *ECLO5a* **(a–g)** and *ECLO4a* **(i–p)**. X-ray maps of **(a)** MnO; **(b)** MgO; **(c)** CaO and LA-ICPMS maps of **(d)** Sm, **(e)** Eu, **(f)** Lu, and **(g)** Ti. Green arrows show the sharp zoning contrast from garnet mantle to rim; white arrows show radial zoning. X-ray garnet maps of **(i)** MnO; **(j)** CaO; **(k)** MgO; **(l)** clinopyroxene X-ray Na_2O maps; and LA-ICPMS maps for of **(m)** Eu, **(n)** Lu, **(o)** V, and **(p)** Dy. The mask file function was used to filter background and inclusions.

2014a; translated from THERMOCALC by Douglas K. Tinkham, 2015) considering a Na_2O-CaO-FeO-MgO-Al_2O_3-SiO_2-H_2O-TiO_2-O_2(Fe^{3+}) system (NCFMASHTO). Estimates of 5 % Fe_2O_3 as FeO_T were based on the best fit between stoichiometric calculations of EPMA mineral data and considered within a 3 %–25 % Fe_2O_3 range. Solution models considered for calculations are from Green et al. (2016) for melt, amphibole, and clinopyroxene; White et al. (2014a) for garnet, orthopyroxene, biotite, white mica, and chlorite; White et al. (2014b) for chloritoid; Holland et al. (2022) for feldspars; White et al. (2000) for ilmenite; and Holland and Powell (2011) for epidote, corundum, kyanite, quartz, zoisite, and rutile. Fluid is assumed to be pure water (H_2O). The proportion of water as fluid phase plays a notable role in the extent of kyanite, amphibole, zoisite and melt stability but is here considered in excess as most dehydration reactions during a prograde evolution under subsolidus conditions would lead to H_2O saturation (Guiraud et al., 2001; Pitra et al., 2022). Geothermobarometry was done using the average P–T module (Av*PT*) in THERMOCALC (database ds55 and software tc345i), which performs a least-squares regression on a set of independent endmember reactions (Powell and Holland, 1994). Activities of end members were calculated using AX (Holland, 2018) from representative analyses identified in Table 1.

3.3 Trace-element maps

Trace-element maps were acquired using LA-ICPMS at the Vegacenter, Swedish Museum of Natural History, Stockholm, Sweden, using an ESI New Wave *NWR193UC* ArF excimer ($\lambda = 193$ nm) LA system coupled to a Nu Instruments *AttoM* high-resolution ICPMS (Fig. 4). The acquisition protocol follows Raimondo et al. (2017). Trace elements were measured in high-resolution mode by analyzing m/z values corresponding to ^{147}Sm, ^{153}Eu, ^{157}Gd, ^{159}Tb, ^{163}Dy, ^{165}Ho, ^{166}Er, ^{169}Tm, ^{172}Yb, ^{175}Lu, as well as ^{51}V, ^{45}Sc, ^{55}Mn and ^{57}Fe. Laser ablation of rectangular spots of 10×10 µm was done at a sample scan speed of 12 µm s^{-1} over an area of 485×420 µm for sample *ECLO4a*. For *ECLO5a*, the same isotopes were measured with additional ^{43}Ca, ^{49}Ti and ^{53}Cr. The map analysis was performed by applying spots of 25×25 µm and a speed of 20 µm s^{-1}, covering an area of 2911×2925 µm. Ablation was performed at a frequency of 20 Hz, 1.5 J cm^{-2} and 0.3 L min^{-1} of He flow rate. NIST612 (rare earth elements, REEs) and BCR2-G (transition metals) were used as primary standard. The analyses were internally calibrated using ^{57}Fe (*ECLO4a*) or ^{43}Ca (*ECLO5a*) as determined by EPMA. Data accuracy was evaluated through repeat analyses of the 8815B as garnet reference material (Kylander-Clark et al., 2007). Data processing and reduction was done using Iolite (Paton et al., 2011, following the protocol from Paul et al., 2012, and Petrus et al., 2017). Post processing was performed using XMapTools 3.4.1 (Lanari et al., 2014, 2019). Figure 4 shows selected trace-element maps for sample *ECLO5a* (Fig. 4d–g) and *ECLO4a* (Fig. 4m–p).

3.4 In situ U-Pb zircon geochronology of the granitic intrusion

Zircon grains were separated from sample *Tregl* from the granitic intrusion in Treglonou orthogneiss. The grains were concentrated by panning from a sieved powder and hand-picked. The grains were mounted in epoxy resin, polished and imaged by cathodoluminescence (CL; CamScan MV2300, 10 kV acceleration voltage, 0.5 nA probe current, 40 mm working distance) at the Earth Sciences Institute (ESI), University of Lausanne, Switzerland. The grains were subjected to U-Pb dating using an Element XR (Thermo Scientific) ICPMS coupled to a New Wave UP193 ArF excimer ($\lambda = 193$ nm) laser system at the ESI. The analyses were performed using a pulse rate of 5 Hz and a laser fluence of ca. 3 J cm^{-2} (Ulianov et al., 2012). Analytical spots of 35 µm were performed in sequential runs of up to 10 unknowns, followed by two measurements for accuracy control (Plešovice natural zircon; Sláma et al., 2008). Each analytical run started and ended with four measurements on the GJ-1 zircon (primary standard; Jackson et al., 2004). The raw data were then processed offline with the LAM-TRACE software (Simon E. Jackson, Macquarie University, Australia, and Jackson, 2008) and plotted using Isoplot/Ex v. 4.15 (Ludwig, 2012). Only concordant ages were considered (Fig. 6, Table S5). Calculated ages are provided at the 2σ uncertainty level. Repeat analyses of the Plešovice zircon (337.13±0.37 Ma, Sláma et al., 2008) yielded 337.4±3.6 Ma (2σ, $n = 19$, mean square weighted deviates MSWD = 0.12; Table S5).

3.5 In situ zircon O, U-Pb and REE analysis

Zircons were identified in five thick sections cut from the two eclogitic samples and imaged using scanning-electron and backscatter-electron (BSE) imaging using Ifremer's FEI Quanta 200 scanning electron microscope operating at 20 kV. Cathodoluminescence imaging (Fig. 7) was performed at the Centre de Recherches Pétrographiques et Géochimiques (CRPG), Nancy, France. Selected areas of a few squared millimeters were then cut, mounted in indium and coated with Au (20 to 30 nm thickness). Oxygen isotope, U-Pb and REE analyses of zircon were carried out at the National Ion Probe facility at CRPG using a CAMECA ims-1270 large-geometry ion microprobe (Fig. 8). The analytical protocols followed are detailed in Deloule et al. (2002) and Jeon and Whitehouse (2015) for U-Pb isotopic analysis, Martin et al. (2006) for oxygen isotope analysis, and Lotout et al. (2023) for trace-element analysis. Sequential analyses of O, U-Pb and REE were performed in this order on, or as close as possible to, each other to ensure optimal correlation

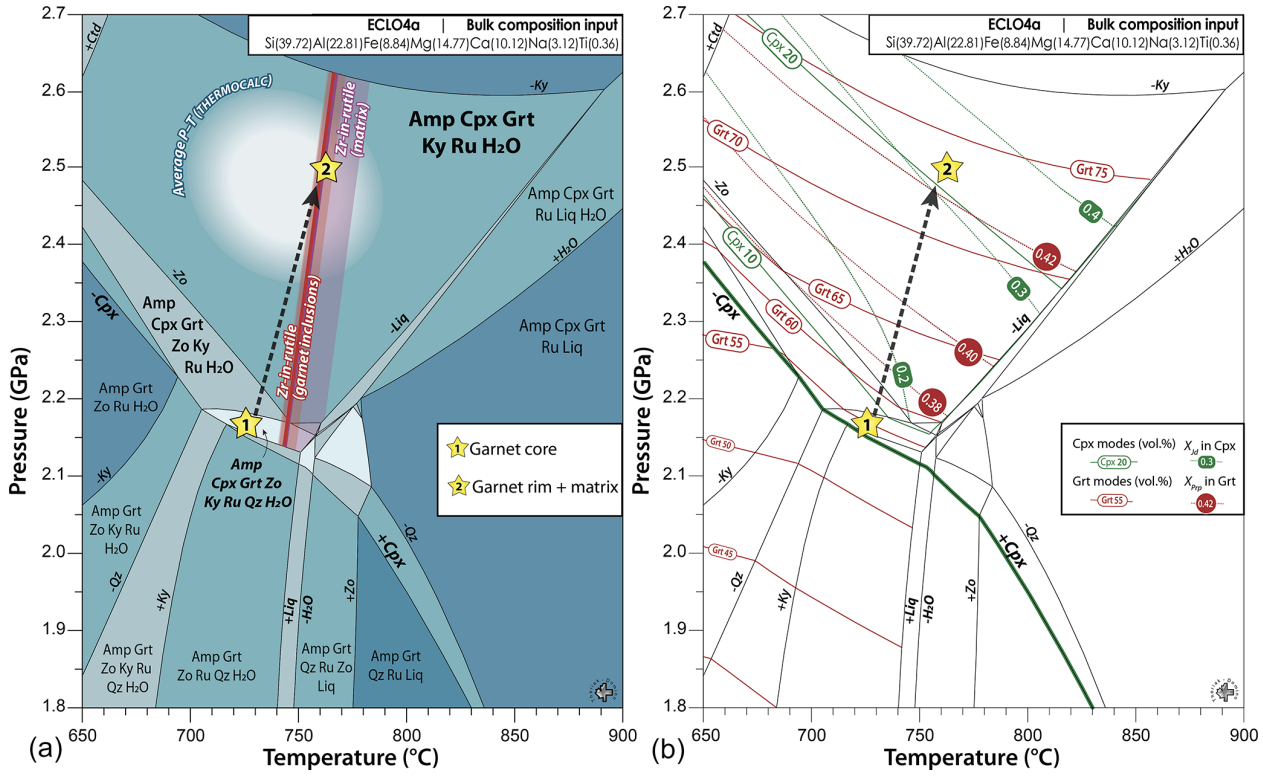

Figure 5. Pseudosection calculated for the kyanite-bearing eclogite (*ECLO4a*). The bulk chemical composition is given as element percent. The dashed arrow indicates the interpreted P–T path from stage 1, i.e., the field assemblage corresponding to garnet core compositions, to stage 2, corresponding to garnet rim assemblage. Average P–T result (Av*PT* Thermocalc) is represented as a white ellipse; median value of Zr-in-rutile in garnet inclusions ($n = 12$) is represented by the red line, and median value of Zr-in-rutile in matrix is represented by the purple line ($n = 21$) (shadowed areas: interquartile ranges). **(b)** Isomodes of garnet and clinopyroxene and isopleths of grossular (X_{Grs}) in garnet and X_{Jd} in clinopyroxene.

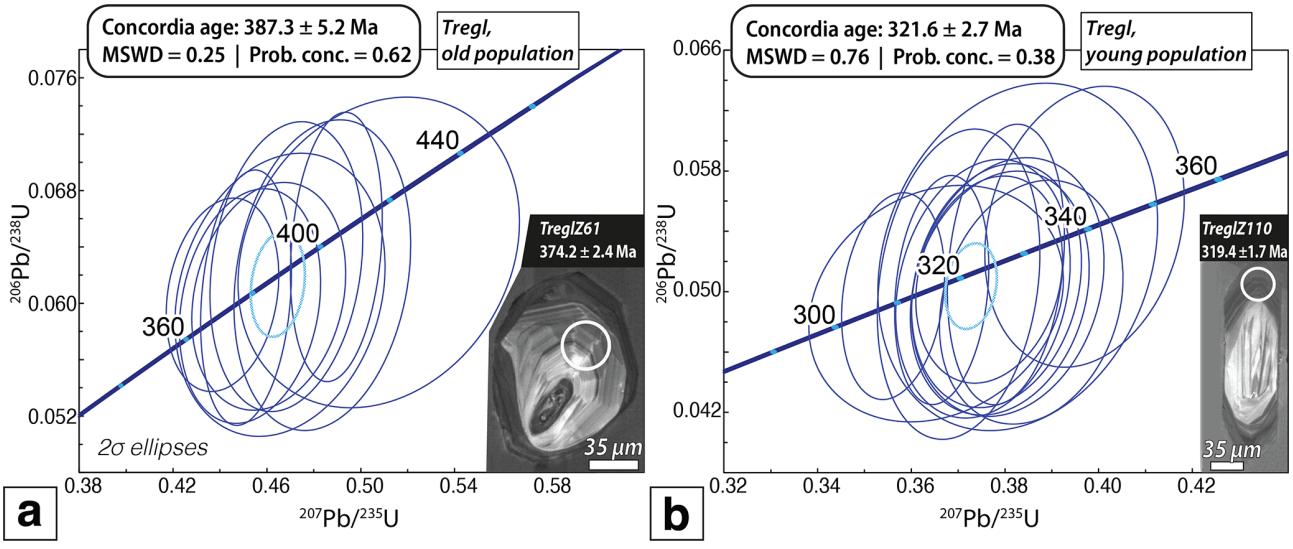

Figure 6. Results of zircon in situ LA-ICPMS U-Pb geochronology from a late intrusion at Treglonou (Sample *Tregl*) showing **(a)** the older, concordant zircon population interpreted as dating magmatic crystallization and **(b)** the younger, concordant zircon population interpreted as dating the partial melting. A representative CL image of each zircon population shows the 35 µm analytical spot and corresponding apparent $^{206}Pb/^{238}U$ age.

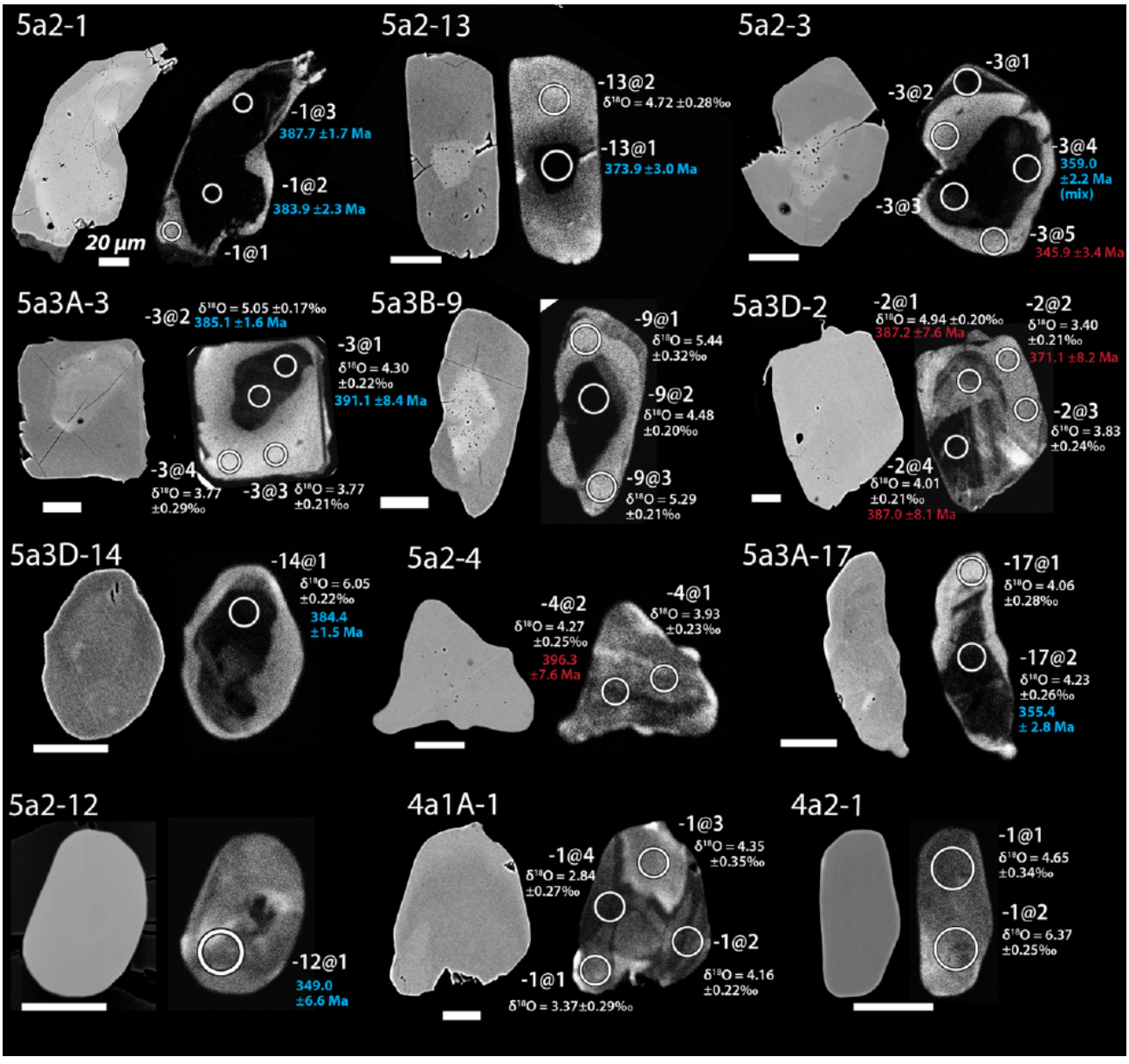

Figure 7. BSE and CL representative zircon grains in the eclogite samples showing analytical spots and corresponding $^{206}Pb/^{238}U$ apparent age (blue: concordant, red: discordant) and $\delta^{18}O$ values. The scale bar is consistently 20 µm wide.

of the results. Full datasets are reported in Tables S1, S2 and S3.

Oxygen isotope analyses were performed in multi-collector mode using a Cs^+ primary ion beam, an acceleration voltage of 10 kV and a beam intensity of 1.9 nA. Forty measurement cycles were acquired on each point. Data were corrected for instrumental fractionation using 91500 reference material (CRPG zircon fragment with a $\delta^{18}O$ value of 10.2 ‰) and reported with $\delta^{18}O$ notation, i.e., in per mil variations relative to the Vienna Standard Mean Ocean Water (VSMOW) and 2σ uncertainties are reported.

Analyses for U-Pb chronology were performed using a O^- primary ion beam, an acceleration voltage of 13 kV and a beam intensity of 5.3 nA. The secondary positive ions were accelerated at 10 kV and analyzed with a mass resolution of 6000 (m/Δm). The measurements were made in mono-collection mode using an ion counter equipped with an electron multiplier. Ten measurement cycles were acquired on each point. Data processing was done following Deloule et al. (2002). The Pb/U ratio was calculated using the $^{206}Pb/UO_2$ ratio as a function of the UO_2/UO ratio measured on the reference material and the samples (Jeon and Whitehouse, 2015). Over the course of the analysis,

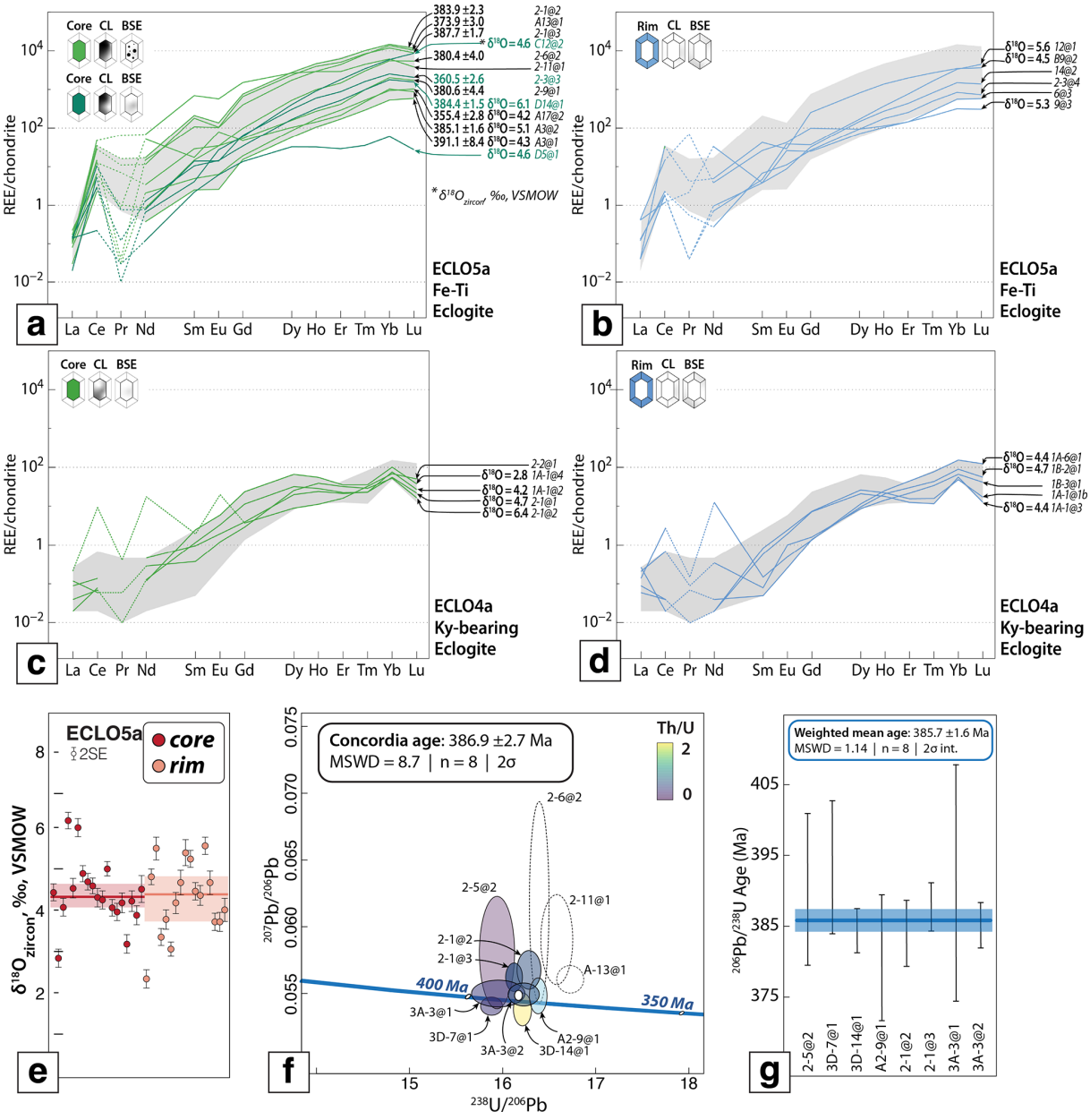

Figure 8. Summary of zircon δ^{18}O, REE and U-Pb results in the eclogites samples. Rare earth element concentrations normalized to chondrite values (McDonough and Sun, 1995) for **(a)** zircon CL-dark cores with and without micro-inclusions in the Fe-Ti rich eclogite *ECLO5a*, **(b)** zircon CL-bright rim in the Fe-Ti rich eclogite *ECLO5a* **(c)** zircon CL-dark core in the kyanite-bearing eclogite *ECLO4a* **(d)** zircon CL-bright rim in the kyanite-bearing eclogite *ECLO4a*. **(e)** Summary of O isotope data in the Fe-Ti rich sample *ECLO5a* (reference lines correspond to the median and shaded domains extend to the lower and upper interquartile ranges of the values). **(f)** Tera–Wasserburg and **(g)** and weighted-mean age diagrams of concordant analyses from CL-dark cores in the Fe-Ti-rich sample *ECLO5a*. Dashed ellipses were not used for the concordia age calculation. MSWD: mean square weighted deviates.

the 91500 zircon (1065 Ma; Wiedenbeck et al., 1995, 2004) was used as a primary reference material. A U-Pb age of 1061.3 ± 3.2 Ma (2σ, $\mathrm{MSWD_{conc+eq}} = 1.8$, $n = 21$) was obtained. The common Pb correction was done on the basis of measured ^{206}Pb/^{204}Pb. Analyses of sample zones with low U concentration (< 1 ppm) were excluded from the calculations. The age uncertainty includes the 2σ analytical error and scatter of the reference analyses combined in quadrature. Concordia plots and U-Pb age calculations were made using Isoplot (Ludwig, 2003).

The concentrations of REEs were measured by applying a primary O^- ion beam (10 nA) and an acceleration voltage at

13 kV. The secondary ions were accelerated at 10 kV and analyzed with a mass resolution of 15 000. Four measurement cycles were acquired for each point. Isobaric interferences were either avoided by measuring the m/z of isotopes free of interference (e.g., ^{139}La, ^{140}Ce, ^{141}Pr) or were monitored by measuring m/z of two isotopes from the same element to deconvolute the interference (e.g., ^{156}Gd, ^{158}Gd). No significant interference from hydrates was detected during analysis. Unknowns were normalized using zircon 91500 (Wiedenbeck et al., 2004), and REE concentrations were normalized to C1 chondrite values of McDonough and Sun (1995; Table S3).

3.6 Garnet Lu-Hf chronology

Eclogite samples were cut into ca. 4 × 3 × 1 cm slabs, which were then hand-crushed using an agate mortar. Garnet grains and fragments were separated under a binocular microscope and weighed in screw-top perfluoroalkoxy (PFA) vials. A ^{176}Lu-^{180}Hf isotope tracer solution with Lu/Hf characteristic of garnet was admixed. Garnet dissolution and spike-garnet equilibrium was achieved by sequential addition of concentrated HF-HNO_3-$HClO_4$ and 6 N HCl interspersed with sample dry-downs on a hotplate. The solutions were then centrifuged, and the dissolved garnet solution was removed by pipetting, leaving behind any refractory minerals such as zircon (Lagos et al., 2007). Isolation of Hf and Lu was done using preconditioned 12 mL Teflon columns containing Eichrom Ln-Spec resin and following the chromatographic procedure of Münker et al. (2001). Both Lu and Hf cuts were purified of Fe^{3+} by reloading with ascorbic acid (Sprung et al., 2010). Garnet-poor rock fragments were processed in an agate mortar and pestle until reaching ca. 150 µm or less. One aliquot of this material was spiked and digested using concentrated HF–HNO_3 in screw-top PFA beakers kept inside steel-jacketed Teflon® digestion vessels at 180 °C for 5 d. A second aliquot was digested using the dissolution procedure as used for garnet. Because subsequent zircon petrochronology revealed high probability of contribution of isotopically unequilibrated refractory minerals (e.g., zircon) on Lu-Hf data, only table-top analyses were used to anchor the isochron. The Lu-Hf analyses were carried out at the Pacific Centre for Isotope and Geochemical Research at the Department of Earth, Ocean and Atmospheric Sciences, University of British Columbia (UBC) in Vancouver, Canada, using a Nu Instruments *Plasma 1* multi-collector ICPMS instrument. Corrections for isobaric interference of ^{176}Yb on ^{176}Lu were done using $\ln(^{176}\mathrm{Yb}/^{171}\mathrm{Yb}) - \ln(^{174}\mathrm{Yb}/^{171}\mathrm{Yb})$ correlations as determined by replicate Yb standard measurements (Blichert-Toft et al., 2002). Mass bias correction for Hf was done assuming the exponential law and applying $^{179}\mathrm{Hf}/^{177}\mathrm{Hf} = 0.7325$. The Hf isotope analyses were normalized to the ATI-475 reference (UBC), which is an in-house-developed Hf isotope reference that is isotopically indistinguishable from JMC-475 and was made from the original metal ingots used in the initial development of that standard ($^{176}\mathrm{Hf}/^{177}\mathrm{Hf} = 0.282160$; Blichert-Toft and Albarède, 1997). The external reproducibility (2 SD) of $^{176}\mathrm{Hf}/^{177}\mathrm{Hf}$ was estimated based on the external reproducibility of ATI-475 measured at concentrations that bracketed those of the unknowns during the course of our analytical sessions (Bizzarro et al., 2003). Isochron regression and age calculation were done using Isoplot version 3.27 (Ludwig, 2003), applying $1.867 \times 10^{-11}\ \mathrm{yr}^{-1}$ for λ^{176}Lu (Scherer et al., 2001; Söderlund et al., 2004). All uncertainties are reported at the 2 SD level. Isotope data and calculated dates are presented in Table 2, and isochrons are shown in Fig. 9.

4 Results

4.1 Petrology and mineral chemistry

The main petrological and chemical characteristics of two eclogitic samples are summarized below. Further details on the petrography are also presented in Cabanis and Godard (1987), Godard and Mabit (1998) and Paquette et al. (1987). Both eclogite types variably preserve HP parageneses, i.e., garnet + omphacitic clinopyroxene + rutile + quartz (Fe-Ti-eclogite *ECLO5a*) and garnet + omphacitic clinopyroxene + kyanite + amphibole + rutile (kyanite-bearing eclogite *ECLO04a*). Although not reported in said studies, our investigation revealed pristine omphacite.

ECLO5a is a Fe-Ti rich eclogite that contains abundant garnet, clinopyroxene (largely replaced by fine-grained diopside + plagioclase symplectites and amphibole), apatite and rutile (largely replaced by ilmenite) (Fig. 2a). Garnet in this sample constitutes 50 % to 60 % of the original paragenesis and contains inclusions of quartz, rutile, apatite, amphibole and former HP clinopyroxene. Rare K-feldspars are also included in garnet associated with amphibole or chlorite (Fig. 3a). Garnet zonation is complex (Figs. 3 and 4) but overall compatible with prograde growth, with a Mn-rich core (4.5 wt % MnO corresponding to X_{Sps}0.1, Table 1) and a progressive increase in MgO and X_{Prp} towards the rim (X_{Prp}0.1 to 0.32). Both MnO and MgO maps in garnet core and mantle show a diffuse zonation, while garnet mantle to rim boundary is sharper (green arrow, Fig. 4). Grossular components (X_{Grs}) are 0.42 to 0.40 in the core and inner rim, and up to X_{Grs}0.62 in the mantle and outer rim. The CaO map shows local enrichments perpendicular to the overall zoning that resemble healed fractures and is particularly visible in the inner rim (Fig. 4c). This feature is also visible on trace-element maps and locally disrupts the overall zoning pattern (white arrows, Fig. 4f, g). The core domain is relatively enriched in middle REEs (MREEs; Fig. 4d, e). The mantle is depleted in light REEs (LREEs) and MREEs, sharply followed by the rim domain characterized by two thin oscillations. The core and mantle are enriched in heavy REEs (HREEs; e.g., Lu up to ca. 15 ppm, Fig. 4f). Concentrations progressively decrease towards the rim. A thin oscillation

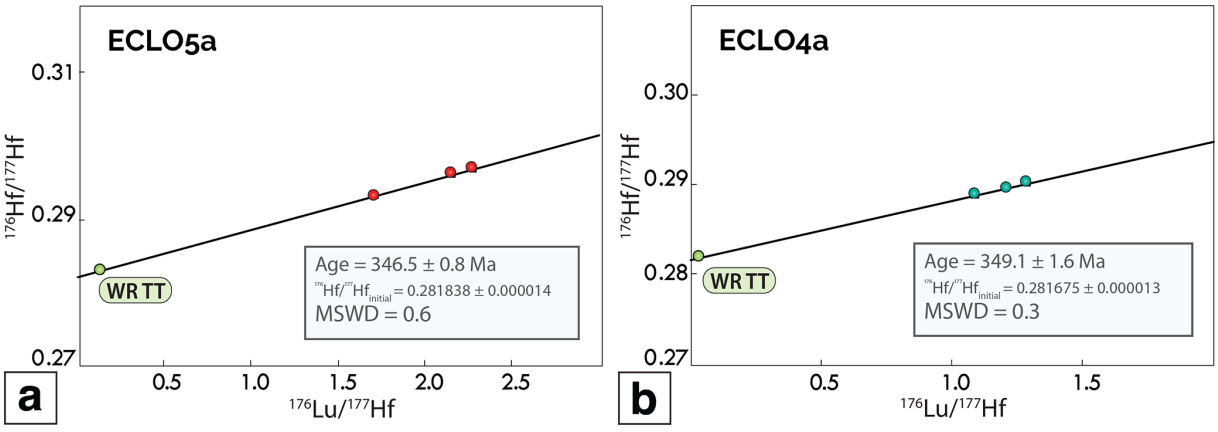

Figure 9. Lu-Hf isochron plots for the eclogite samples. **(a)** Isochron for the Fe-Ti-rich eclogite *ECLO5a* ($n = 4$), **(b)** Isochron for the kyanite-bearing sample *ECLO4a* ($n = 4$). Red and blue dots correspond to garnet aliquots; green dots correspond to their respective garnet-depleted whole-rock aliquots. Data point including estimated 2 SD corresponding uncertainty are smaller than their respective marker. WR TT: garnet-poor whole rock following a table-top dissolution procedure.

is visible in the outer rim (Fig. 4f) and corresponds to the sharp oscillation in LREEs and MREEs. The transition from the core to this outer rim oscillation shows a strong radial component (white arrow, Fig. 4f). Garnet shows a sharp decrease in Ti between the large core and mantle domains (up to 1500 ppm) and the rim (200 ppm; Fig. 4g); local Ti enrichment is also visible around amphibole and rutile inclusions.

Clinopyroxene makes up ca. 30 % of the original paragenesis. Former omphacite is now largely replaced by diopside + plagioclase (see Cabanis and Godard, 1987, for extended symplectites description) and tschermakite to magnesio-hornblende amphibole (Figs. 2a, 3g). Apatite is abundant in the sample and is found as large inclusions (up to 500 µm) in former clinopyroxene and garnet (Fig. 2a). Rutile constitutes up to 10 % of the original paragenesis and is found as inclusions in garnet and clinopyroxene. Former large rutile matrix grains (ca. 500 µm) are largely replaced by ilmenite (Fig. 2a). Minute ilmenite grains are also found as inclusions in garnet. Small zircon grains (< 100 µm) occur as inclusions in major minerals (garnet, clinopyroxene and symplectites) and in the matrix.

ECLO4a comprises a fine-grained assemblage of garnet + clinopyroxene + amphibole + rutile ± zoisite. The assemblage is well-preserved, with only minor replacement by symplectites along grain boundaries. Garnet represents ca. 40 % of the rock, is fine-grained (ca. 0.5 mm) and is typically surrounded by a thin corona of amphibole + plagioclase (Fig. 2b). Garnet contains rare inclusions, mostly made of quartz and rutile and minor kyanite, clinopyroxene, and amphibole (Fig. 2b). Garnet shows minor zoning in X_{Sps} (0.1–0.2) and generally shows anti-correlated zoning for X_{Prp} (ranging 0.32–0.44) and X_{Grs} (ranging 0.15–0.23), with higher X_{Grs} components in the core and an inner rim. Core domains are poor in HREEs and are surrounded by a micrometer-scale annulus enriched in HREEs and a rim depleted in HREEs. The MREEs (Fig. 4m) show very low concentrations in the core (e.g., Dy < 1 ppm). Concentrations progressively increase towards the rim, peaking at ca. 6 ppm in the outermost rim. Overall, the REE concentrations in garnet are very low, with Lu (Fig. 4o) reaching only 3.5 ppm in the annuli. The concentrations of V and Sc are typically low in the garnet core and progressively increase towards the rim (Fig. 4p).

Clinopyroxene has a bright green color in hand samples and is up to a few millimeters across; it is the second-most abundant mineral after garnet and constitutes ca. 35 %–40 % of the original paragenesis (Fig. 2b, c). Compared to matrix clinopyroxene described for the Léon kyanite-bearing eclogite in the literature, clinopyroxene in *ECLO4a* locally preserves omphacitic compositions. Highest jadeite components (X_{jd} 0.30–0.40) occur in the core of grains (Figs. 3i and 4j). Clinopyroxene grains contain inclusions of large amphibole, kyanite and rare quartz (Fig. 2c) and are partly replaced by a symplectite of diopside + plagioclase along grain boundaries. In these symplectites, diopside typically has X_{jd} of 0.07 or less. Kyanite represents about 5 %–10 % of the original paragenesis and is surrounded by a 100–200 µm symplectite of sapphirine + plagioclase ± corundum ± spinel intergrowth (Fig. 3f, j). Individual grains of sapphirine are usually a few micrometers across and have X_{Mg} of ca. 0.5. Plagioclase is strongly zoned away from kyanite. Microscopic zones enriched in Na occur at the boundary between kyanite symplectites and omphacite. Corundum and spinel are rare and only a few micrometers wide. They both constitute intergrowth with plagioclase symplectites near garnet and kyanite symplectites (Fig. 3f). Amphibole occurs as large inclusions in clinopyroxene (up to a few hundreds of micrometers) and garnet, and as symplectites around garnet (Fig. 3f). Amphibole in clinopyroxene is magnesio-hornblende, whereas symplectitic and retrograde

amphibole are pargasite to sadanagaite (Fig. 3g; Leake et al., 2004). Zoisite constitutes ca. 5 % of the original paragenesis; it occurs as rounded grains included in clinopyroxene, kyanite or as matrix grains (200 µm wide) adjacent to garnet. Locally, a fine-grained (µm-scale) overprinting texture made up of white mica + plagioclase developed at the rim of zoisite. It is difficult to determine whether this texture developed just before or after the peak assemblage as it is also locally visible on zoisite inclusions included in omphacite. Rutile is a common accessory phase found as inclusion in garnet and clinopyroxene and can be up to a few hundreds of micrometers in the matrix. Zircon and sulfide minerals occur as accessory phases in the matrix and major minerals; sulfide phases contain variable concentrations of Fe, Cu and Ni.

4.2 *P–T* estimates

The pseudosection for the ky-bearing eclogite (*ECLO4a*) reproduces the paragenesis found as inclusion in garnet (field garnet + kyanite + clinopyroxene + zoisite + quartz + amphibole + rutile) at ca. 2.2 GPa and 700–750 °C (Fig. 5a). This first-order observation can be used to interpret this field as the maximum *P–T* conditions corresponding to garnet core. The field that corresponds to the garnet rim and matrix assemblage, which is characterized by a significant growth of jadeite-rich omphacite and kyanite (field garnet + kyanite + clinopyroxene + amphibole + rutile), extends up to 2.6–2.7 GPa and 850 °C. Several lines of evidence can be used to refine the *P–T* peak conditions. Firstly, the modal proportion of omphacite is ca. 40 vol. % in the area from where the bulk composition was extracted and thus requires us to significantly exceed the conditions of the cpx-in-line modeled at 2.2 GPa and 700–750 °C (Fig. 5b). Modeled compositional values of X_{Jd}(0.3 to 0.4) are consistent with measured values and are found in the peak *P–T* field between 2.4 and 2.6 GPa – a field that also match measured X_{Prp} values in garnet rim (0.42–0.44). However, it has to be noted that measured cpx modal proportions are higher than those modeled in the pseudosection. Secondly, *P–T* estimates using Av*PT* in Thermocalc, which were made on representative analyses of garnet mantle and the inclusion or adjacent assemblage interpreted to be contemporaneous (i.e., garnet + omphacite + kyanite + zoisite + amphibole + rutile), yielded peak conditions of 2.6 ± 0.2 GPa and 750 ± 60 °C (cor.: −0.158; sigfit: 1.95; Fig. 5) from eight independent reactions (Fig. 5a, white ellipse). Zoisite was considered in Av*PT* calculation because the mineral is present as inclusions in kyanite, clinopyroxene and garnet (Fig. 2b, c), while the pseudosection predicts zoisite breakdown before the *P–T* peak conditions. Thirdly, the *T* estimated independently using Zr-in-rutile thermometry can be used to further refine the peak *P–T* estimates. Thirty-three analyses were performed in garnet inclusions ($n = 12$) and the matrix ($n = 21$) (Table S4 in the Supplement, reported as red and purple lines in Fig. 5a). At 2.0–2.5 GPa, Zr-in-rutile *T* estimates from in-

Table 2. Summary of the Lu-Hf geochronology results.

Sample	Zone	Lu ($\mu g\,g^{-1}$)	Hf ($\mu g\,g^{-1}$)	$^{176}Lu/^{177}Hf$	2 SD	$^{176}Hf/^{177}Hf$	2 SD	$^{176}Hf/^{177}Hf_{initial}$	2 SD	Lu-Hf age (Ma)	2 SD	MSWD
ECLO5a	Grt-1	2.160	0.178	1.7180	0.0043	0.292965	0.000039	–	–	–	–	–
	Grt-2	2.230	0.146	2.1600	0.0054	0.295860	0.000027	–	–	–	–	–
	Grt-3	2.050	0.127	2.2790	0.0057	0.296640	0.000036	–	–	–	–	–
	WR-1 TT	0.792	0.832	0.1349	0.0003	0.282714	0.000014	–	–	–	–	–
	All aliquots							0.281838	0.000014	346.5	0.8	0.56
ECLO4a	Grt-4	0.675	0.079	1.2070	0.0030	0.289632	0.000084	–	–	–	–	–
	Grt-1	0.710	0.092	1.0890	0.0027	0.288801	0.000039	–	–	–	–	–
	Grt-2	0.770	0.085	1.2900	0.0032	0.290102	0.000037	–	–	–	–	–
	WR-1 TT	0.123	0.500	0.0348	0.0001	0.281903	0.000013	–	–	–	–	–
	All aliquots							0.281675	0.000013	349.1	1.6	0.28

Note: Grt: garnet; MSWD: mean square weighted deviates; SD: standard deviation. WR TT: whole-rock dissolution procedure as table top (TT).

clusions in garnet are 740–760 °C. For matrix grains, T estimates are 750–780 °C, assuming the same P. These T values are similar, although rutile included in garnet shows more restricted ranges. As quartz is not present in the garnet rim and matrix assemblages, there is a possibility that $a_{Si} < 1$, and these calculations would therefore represent *maximum* T (Zack et al., 2004). Together, the Zr-in-rutile pseudosection modeling and Av*PT* calculations thus indicate that peak T conditions were 750–780 °C and ca. 2.5 GPa and that T remained around 740–770 °C during decompression.

4.3 Chronology

4.3.1 U-Pb dating in zircon from the Treglonou magmatic intrusion

Zircon in the *Tregl* sample dominantly shows S1, S12 and S2 morphologies (cumulating 47 % of the 234 grains observed), with secondary morphologies of S17, S7, S6 and S11 types (cumulating 28 % of the grains). These morphologies are consistent with a crustal origin (Pupin, 1980). The crystals are translucent, colorless and elongated (2 : 1 to 3 : 1), with growth zoning sometimes visible under natural light. The U-Pb analysis provided concordant ages between 416 to 309 Ma, with a gap of ages between 375–340 Ma (Table S5; Fig. 6). The dataset suggests the presence of two populations: an older population at 387.3±5.2 Ma ($n = 9$, MSWD = 0.25, probability of concordance = 0.62; Fig. 6a), which was mostly seen in zircon bright-CL cores, and a younger population at 321.6 ± 2.7 Ma ($n = 13$, MSWD = 0.76, probability of concordance = 0.38; Fig. 6b), as mostly seen in dark-CL rims.

4.3.2 In situ zircon petrochronology of the eclogites

Zircon grains in *ECLO5a* are small (generally ca. 50 µm; Fig. 7) and rounded to slightly elongated and small (generally ca. 50 µm; Fig. 7). The grains show consistently dark-CL and bright-BSE cores containing micro-inclusions and are sometimes associated with slightly brighter domains in BSE (Fig. 7). Rims are thin (< 15 µm), CL bright and slightly darker in BSE than the cores. A CL-dark outer rim that is a few micrometers thick is visible on a few grains (e.g., 5A2-3, 5a3B-9, Fig. 7) as well as healed fractures, very bright in CL. In *ECLO4a*, zircon grains are rare and smaller than in *ECLO5a* (mostly < 40 µm) but show similar CL zoning with CL-dark zones in the core and bright rims. Zircon cores that are slightly brighter in CL (Fig. 8a) are generally depleted in REEs compared to dark-CL, micro-inclusion-rich cores. Apart from one analysis, zircon does not show a Eu anomaly. The most REE-depleted zircon also provided the youngest ages (< 360 Ma, discordant apparent ages, Table S1). Analyses of zircon rims (Fig. 8b) were mostly mixed due to their width, which is generally below spot size. The rims show apparent, discordant younger ages and are HREE-depleted. Zircon grains in *ECLO4a* (Fig. 8c–d) are overall an order of magnitude more depleted in REEs than zircon in *ECLO5a*. Both core and rim domains are generally HREE-depleted, show no Eu anomaly and have MREE-depleted rims. The $\delta^{18}O$ values for zircon in both samples are consistently below 6.5 ‰, both in core and rim domains (Fig. 8e; Table S2). The data for *ECLO5a* ($n = 37$) show median values at 4.3 ‰ in cores, with a restricted interquartile range (IQR: 4.1 ‰–4.7 ‰), and 4.4 ‰ (IQR: 3.7 ‰–4.8 ‰) in rims. The five analyses obtained in *ECLO4a* are consistent with these values (Table S2). These values are largely below mantle zircon values (5.3 ± 0.6 ‰ 2 SD; Valley et al., 1998). Only three U-Pb analyses were attempted in zircon from *ECLO4a*; they yielded discordant analyses and are not further discussed. Zircon dark-CL cores in *ECLO5a*, which are often associated with micro-inclusions, consistently show a minor negative Eu anomaly (Fig. 8a). Apparent $^{206}Pb/^{238}U$ ages are between 400–375 Ma. Eight concordant analyses of dark-CL cores (seven of which associated with micro-inclusions) from sample *ECLO5a* yield a concordia age of 386.9 ± 2.7 Ma (MSWD concordance + equivalence = 8.7; Fig. 8f). The same analyses yielded a weighted mean $^{206}Pb/^{238}U$ age of 385.7±1.6 (MSWD = 1.1; Fig. 8g). Only three younger concordant ages were obtained from *ECLO5a*: a dark outer core that appear to mixed with the rim ($^{206}Pb/^{238}U$ age = 355.4 ± 2.8 Ma; Fig. 7), a second one from a zircon CL-dark overgrowth ($^{206}Pb/^{238}U$ age = 359.0 ± 2.2 Ma; Fig. 7) and third one from a zircon CL-medium-bright rim (349.0 ± 6.6 Ma; Fig. 7; Table S1).

4.3.3 Garnet Lu-Hf analysis

Consistent with observations from trace-element mapping in garnet, garnet aliquots used for geochronology have very low Lu concentrations in *ECLO4a* (0.7–0.8 ppm, Table 2) and slightly higher concentrations in *ECLO5a* (2–2.2 ppm). For both samples, Lu-Hf isochrons were calculated from the garnet and garnet-depleted rock analyses. A Lu-Hf age of 346.5 ± 0.8 Ma (MSWD = 0.56, Fig. 9a) was obtained for *ECLO5a* and an age of 349.1 ± 1.6 Ma (MSWD = 0.28, Fig. 9b) was obtained for *ECLO4a*.

5 Discussion

5.1 The age and composition of the protolith

Zircon in *ECLO5a* reveals an initial growth stage that consistently corresponds to a pattern of dark-CL/light-BSE cores, generally containing abundant micro-inclusions. These core domains typically show enriched-HREE profiles and typical negative Eu anomalies consistent with magmatic zircon that crystallized in the presence of plagioclase (Fig. 8a, c; e.g., Rubatto, 2002). Bright-CL rims are generally thin and were rarely large enough to be analyzed. Three analyses show, however, a slight depletion in HREEs, and two show a positive anomaly in Eu that may be consistent with the break-

down of plagioclase occurring during prograde metamorphism (Fig. 8b, d). Fewer analyses were possible in *ECLO4a* due to the low abundance and small size of zircon overall. Except from a slight depletion in MREEs, no distinctive features in the REE pattern can be identified between core and rim domains of zircon in *ECLO4a*.

The core domains of zircons in the eclogite samples show low δ^{18}O values (Fig. 8e, Table S2) that are below typical mantle values (5.3 ± 0.6 ‰, 2 SD; Valley et al., 1998). Crystallization of the eclogite protolith magma from a metasomatized mantle – resulting from interaction with high-temperature, low-δ^{18}O metasomatic fluids associated with serpentinization – could account for δ^{18}O values below 5 ‰. However, this scenario would imply unusually intense metasomatism during protolith formation, as such fluids typically exhibit minimum δ^{18}O values of 3 ‰ (Rubatto, 2017). Assimilation of low δ^{18}O magma (Reimink et al., 2014) during the eclogite protolith's crystallization is considered unlikely due to the absence of pre-385 Ma inherited zircon and the juvenile whole-rock Nd signature (Paquette et al., 1987). Alternatively, low δ^{18}O values are also found in basalts from hydrothermally altered ocean-floor and rift zones and interpreted to reflect relatively shallow crustal interaction with meteoric waters at high T (Bindeman, 2008). This would require the protolith magma to emplace at shallow levels and/or the presence of a major detachment and fracture networks to serve as meteoric fluid pathways, such as commonly found in slow-spreading oceans or immature back-arcs (e.g., Boschetti et al., 2023). The presence of fluids is corroborated by the abundance of micro-inclusions in dark-CL domains and is our preferred interpretation.

Only one concordant age was obtained from zircon in *ECLO4a* due to the few and extremely small size of the zircon, therefore ages interpretation in zircon from the eclogite are discussed based on zircon from sample *ECLO5a*. The concordia age of 386.9 ± 2.7 Ma (MSWD = 8.7, uncorrected for common Pb) and weighted mean $^{206}Pb/^{238}U$ age at 385.7 ± 1.6 Ma (MSWD = 1.14) obtained for eight analyses of dark-CL cores of zircon in sample *ECLO5a* (Fig. 8f–g) likely represent the protolith, given that they are the oldest age component in the eclogites and zircon with these ages shows magmatic REE signatures. The protolith age is contemporaneous with the age of the enclosing Treglonou and Plounévez-Lochrist monzogranitic orthogneisses (391 ± 7 Ma; Marcoux et al., 2009), which are also consistent with the older of two age populations obtained from sample *Tregl* (387.3 ± 5.2 Ma, Fig. 6b).

Zircon mantles and rims record a subsequent event. Only one concordant age was obtained for a CL-medium bright rim in *ECLO5a* zircon and yielded a $^{206}Pb/^{238}U$ age of 349.0 ± 6.6 Ma (Fig. 8b; Table S1), consistent within error with the Lu-Hf ages. This concordant analysis indicates that zircon rim is likely related to prograde to near-peak metamorphism and discordant analyses represent partly mixed domains due to their very limited size. During HP metamorphism, the system likely remained partly closed, as most rim analyses have similar δ^{18}O values to the core, although a few rim analyses plot above 5 ‰ (Fig. 8e).

5.2 Peak metamorphic conditions

Each method used for P–T estimates (pseudosection modeling, Av*PT* and Zr-in-rutile) presents specific limitations. Estimates of bulk compositions were done on the basis of element maps, which provide a 2D representation of the rock volume. The area nevertheless covers a relatively large domain with respect to the grain size, in which case the associated uncertainty using a Monte Carlo approach is small and unlikely to significantly affect the observed field assemblages (Lanari and Engi, 2017). There is an inherent uncertainty in estimating the exact modal proportion of each phase due to the symplectites, but the original corresponding phases can still be approximated and do not impact the following interpretations. Although phase isopleths obtained in pseudosection calculation are not sufficiently thermodynamically constrained to be used as an absolute quantitative tool, it is noted that X_{Jd} in clinopyroxene and X_{Prp} calculated in the peak field in garnet are consistent with our analyses (Fig. 5b). Modal proportions of garnet and amphibole in the pseudosection model are nevertheless overestimated by ca. 15 % for garnet and ca. 8 % for amphibole, whereas omphacite modal proportions are underestimated by ca. 8 %. The sample appears well-equilibrated at HP, with little to no change in T recorded by rutile and very limited X_{Jd} zoning in omphacite. To test whether estimated mineral proportions are off due to the possible effect of garnet fractionation, we fractionated ca. 98 % of garnet at conditions of 2.1 GPa and 700 °C. This operation significantly widened the kyanite- and zoisite-bearing fields, which may be consistent with the presence of large zoisite in clinopyroxene. Garnet fractionation results in garnet modal proportions decrease in the field garnet + clinopyroxene + amphibole + kyanite + zoisite + quartz + rutile compared with the original bulk composition model. It also results in an increase in estimated clinopyroxene and amphibole modal proportions (e.g., at 2.18 GPa 740 °C: new garnet 3 vol. %; amphibole 75 vol. %, clinopyroxene 6.5 vol. %, zoisite 11 vol. %, kyanite 2 vol. %). At 2.5 GPa 760 °C, part of the resulting modes appear more accurate as kyanite reaches 3.5 vol. % and garnet makes up a total of ca. 60 vol. %. Amphibole is nevertheless exceedingly abundant (21 vol. %) and clinopyroxene abundance is even lower than when using unfractionated compositions (16 vol. %). Additionally, clinopyroxene composition is diopside with $X_{Jd=0.2}$, and garnet has low X_{Alm} values (0.2) but high X_{Prp} (0.5) and X_{Grs} (0.27). Although the exact timeline and proportion of mineral fractionation is difficult to constrain, the unfractionated garnet bulk composition yields the best fit overall and is therefore favored for further discussion. The P–T peak reached by the eclogite is therefore best estimated at ca. 2.5 GPa and 760 °C. This re-

sult is significantly higher than previous minimal estimates of 1.3–1.4 GPa at 650–700 °C using conventional thermobarometers (Cabanis and Godard, 1987; Paquette et al., 1987; Godard and Mabit, 1998). The main reason for these discrepancies lies in the fact that only extensively retrogressed eclogite has been described so far. Previous estimates were based on a few omphacite inclusions with X_{Jd} ca. 25 mol %, which contrasts with the fresh eclogite described here that contains abundant, large and preserved matrix omphacite with consistent X_{Jd} of 35 mol %–40 mol %.

5.3 Processes, conditions and age of garnet growth

Garnet zoning from core to rim in *ECLO5a* undoubtedly reflects prograde growth overall, best reflected through compatible-rich elements in garnet core that progressively decreases towards the rim. Garnet core and mantle growth, however, resembles "branched" garnet of Wilbur and Ague (2006), which is interpreted to reflect intense, accelerated bursts of garnet growth following overstepping. These bursts of core–mantle nucleation in *ECLO5a* are separated by a sharp contrast in major-element and trace-element zoning that is compatible with a growth hiatus (green arrow, Fig. 4d–g). The preservation of such zoning reflects high-energy growth. The garnet rim must, nevertheless, have grown shortly thereafter to prevent complete smoothing of the anhedral pattern in major elements (Wilbur and Ague, 2006). Within this second burst of garnet growth to rim crystallization (Fig. 4), fluctuations in REEs occur and may be consistent with fluid-saturated growth (Konrad-Schmolke et al., 2023; Smit et al., 2024; George et al., 2024; Tual et al., 2025). The transition from small ilmenite inclusions in garnet core and mantle to large rutile inclusions in garnet rims coincides with the transition between high Ti concentrations in the core–mantle domain and low Ti concentrations in the garnet rim (green arrow, Fig. 4g). Both changes record prograde ilmenite breakdown in a Fe-Ti-rich sample being buried to eclogite-facies conditions, similar to the one observed in Tual et al. (2018). Garnet grains in *ECLO4a* are extremely abundant, which may partly explain the generally low concentrations of garnet-compatible elements such as Mn and HREEs. The presence of annuli in garnet-compatible elements such as Mn and HREEs around an angular core domain may reflect sequestration and later release of these elements due to the presence and breakdown of other phases (e.g., Rubatto et al., 2020) or may indicate changes in the garnet growth pace (e.g., George et al., 2018) – or a combination of both. Zoisite breakdown is predicted to occur during the P increase from stage 1 to stage 2 in the pseudosection (Fig. 10). This breakdown would yield a MREE enrichment combined with an increase in CaO – a feature that is observed in the zoning of garnet rims outside of the HREE-rich annuli in *ECLO4a*.

The garnet Lu-Hf ages almost overlap within uncertainty, differing effectively only by 0.2 Myr. In both cases, the garnet Lu-Hf ages provided age estimates for the processes causing garnet growth in both samples. In *ECLO5a*, the age is likely biased towards the core, where bulk-grain Lu budgets are highest. In the case of *ECLO4a*, any bias would be towards the mantles, which are Lu-rich, and the rims, which are volumetrically the largest. Garnet growth in both samples nevertheless occurred as part of the HP metamorphic stage of the lens in which the rocks occur. The following observations are relevant in the context of garnet age interpretation: (1) the ages are similar and (2) the age of *ECLO5a* is actually younger than that of *ECLO4a*, even though any bias in the latter sample would be towards the high-grade rims associated with HP zoisite breakdown. On the basis of these observations, it is suggested that both ages date garnet growth close to peak conditions and that the age for *ECLO5a* may reflect the presence of a significantly younger overgrowth that may have formed after reaching these conditions.

The age of HP metamorphism as constrained by Lu-Hf in garnet is much younger than the age obtained from 50 mg of zircon grains extracted from ca. 130 kg of a Fe-Ti rich eclogite sample by Paquette et al. (1987; 439 ± 12 Ma). Three zircon populations, divided by size, were dissolved and analyzed, yielding three data points with said age as lower intercept. Paquette et al. (1987) report zircon grains lacking CL zoning, which strongly differs from our observations, as all observed zircon, in both samples, were consistently and conspicuously zoned. The age was interpreted to represent eclogite-facies metamorphism but actually is older than all ages obtained here, including that taken to represent the eclogite protolith. The U-Pb age obtained for the protolith (concordia age 386.9 ± 2.7 Ma with MSWD = 8.7; weighted mean age at 385.7 ± 1.6 Ma with MSWD = 1.14; Fig. 8f–g) was obtained from (1) consistent textural core domains in zircon (CL dark, largely showing micro-inclusions) corresponding to (2) consistent $\delta^{18}O$ values and (3) REE patterns. The new Lu-Hf and U-Pb data provide a significance advance and fundamentally different picture regarding the age record of the Léon eclogites, which enables a re-evaluation of the role and meaning of these rocks in the Variscan framework.

Exhumation

The younger of the two age data from the Treglonou orthogneiss (321.6 ± 2.7 Ma, Fig. 6c) is interpreted as the age of partial melting and deformation. This anatexis is contemporaneous with extension processes occurring in the region and is a typical process associated with migmatitic dome exhumation. The result demonstrates that the dome extrusion occurred around 320 Ma, which is synchronous with the emplacement of Saint-Renan granite and the Groac'h Zu diorite and with the migmatites of Plouguerneau (330 ± 9 Ma, Marcoux et al., 2009 – TIMS U-Pb on zircon; 311 ± 14 Ma, Schulz, 2013 – EPMA U−Th/Pb on monazite) and Kerhornou (325 ± 5 Ma; Faure et al., 2010 – EPMA U−Th/Pb on monazite) (Fig. 10a). This extrusion event facilitated the exhumation of the eclogite and is likely responsible for the

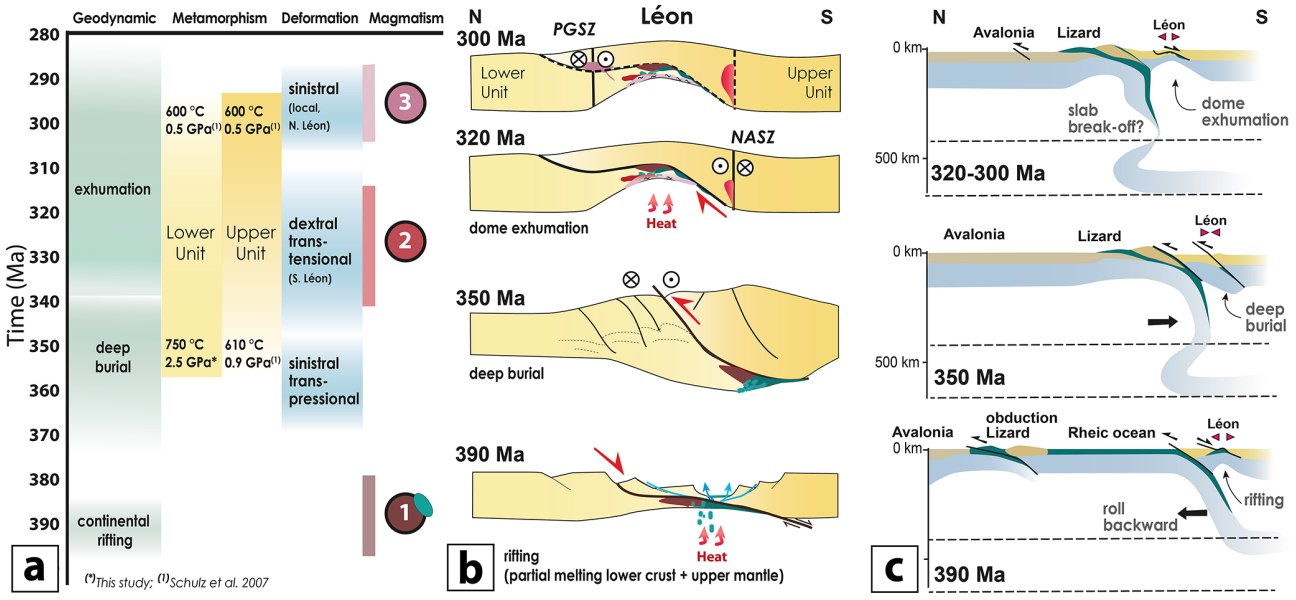

Figure 10. Summary of geological timeline and tectonic interpretations from ca. 400 to 300 Ma. **(a)** Major geodynamic, metamorphic, structural and magmatic events recorded in the Léon Domain. Magmatic phases corresponds to (1) Tréglonou and Plounévez-Lochrist gneiss and eclogite protoliths (this study; 391 ± 7 Ma in Marcoux et al., 2009, TIMS U-Pb on zircon); (2) Tréglonou intrusion (this study), Groac'h Zu and Saint-Renan (318 ± 2 Ma and 316 ± 2 Ma; Le Gall et al., 2014, LA-ICPMS on zircon), Kerhornou and Plabennec (325 ± 5 Ma and 331 ± 6 Ma; Faure et al., 2010, EPMA U−Th/Pb on monazite), Kersaint and Plouguerneau (331 ± 4 Ma and 330 ± 9 Ma; Marcoux et al., 2009, EPMA U−Th/Pb on monazite); (3) Aber Ildut Complex (290 ± 5 Ma, 304 ± 1 Ma, 303.8 ± 1 Ma; Caroff et al., 2015, LA-ICPMS on zircon). **(b)** Schematic cross-section of the Léon Domain at crustal scale showing a reconstruction of the major features recorded and summarized in **(a)**. **(c)** Interpreted large-scale cross-sections for the Léon Domain within the Rheic subduction system adapted from Boutoux et al. (2021): the Mid Devonian stage (ca. 390 Ma) is characterized by a rifting and detachment in the Léon Domain synchronous with obduction of the Lizard ophiolites, compatible with a retreating slab. The early Carboniferous stage (ca. 350 Ma) corresponds to the HP stage in the Léon Domain, compatible with a trench advance that triggered the rift inversion and associated with a sinistral transpression. This likely corresponds to the final suture of the main Rheic Ocean. The Early Carboniferous stage (320–300 Ma) corresponds to either a trench retreat or slab break-off that drives extension, migmatization of the lower crust and dome formation in the Léon Domain.

extensive retrogression observed in the vast majority of the eclogite samples, which is particularly pronounced in eclogites occurring near the Treglonou migmatites.

5.4 Regional implications: source and significance of the eclogite

The new results place robust and precise P–T–t constraints in the history of the Léon Domain and call for a revision of existing models. At 390–385 Ma, a rifting event caused bimodal magmatism that produced monzogranitic Treglonou and Plounévez-Lochrist orthogneisses. The N-MORB tholeiitic precursor of the eclogites – one with a Mg-rich composition (*ECLO4a*-type) and another with Fe-Ti enrichment (*ECLO5a*-type) – likely represented cumulate or residual melt derived from mantle magmatism (Cabanis and Godard, 1987; Paquette et al., 1987). Whether the now lens-like eclogite bodies represent initial igneous bodies or whether they are tectonic fragments of larger, more coherent mafic intrusions is not clear. The absence of pre-385 Ma inherited zircon, the juvenile Nd signature (Paquette et al., 1987) and low δ^{18}O values (ca. 4.2 ‰) in zircon nevertheless indicate emplacement without significant interaction with continental crust. Additionally, the low δ^{18}O (ca. 4.2 ‰) values in zircon impose the emplacement of the mafic protolith at shallow crustal depth or in a context where a large-scale shear zone creates deep fluid pathways for meteoric water. These features could indicate a mantle source situated just below rather than in a distal ridge system. The emplacement setting of the protolith of the Léon eclogites thus may represent a restricted rifting zone with bimodal crust and mantle magmatism caused by asthenospheric ascent (Fig. 10b).

The new data may bear significance beyond the Léon Domain, e.g., for the nearby Lizard Complex. The proposition that this complex represents a short-lived rift inverted starting shortly after 400 Ma followed by a subduction that likely continued southwards (Nutman et al., 2023) is compatible with the recent re-interpretation of seismic data indicating a strong discontinuity that may represent such a suture ("Intra-Saxothuringian suture" in Schulmann et al., 2022) and corroborates previous interpretations that the Lizard Complex does not represent the final Rheic suture (e.g., Floyd, 1984; Cook et al., 2002; Leveridge and Shail, 2011: Alexander et

al., 2019). Based on these interpretations and the new data provided here, a new large-scale tectonic model can be proposed (Fig. 10c). In this model, the Lower Unit of the Léon Domain represents part of a rift that developed as a back-arc of the main Rheic subduction. We propose that the rift was originally associated with a lithospheric-scale detachment zone, which was inverted to allow for deep burial of the Léon eclogites and focusing of deformation in this system, rather than across a broader nappe system for which there is no evidence in the region (Schulz et al., 2007). A similar consequence may be the inversion and northerly directed thrusting, which started shortly after 400 Ma in the Lizard Complex and caused obduction of the ophiolite at ca. 390 Ma (Nutman et al., 2023). Both events can be unified in a single process of slab retreat within the main Rheic subduction tract (Fig. 10c). The eclogite-bearing Léon Domain, i.e., the Lower Unit, was subsequently buried to depths equivalent to 2.5 GPa (likely ca. 80 km) and 760 °C, which require inversion of the rift in the Léon Domain at or before ca. 350 Ma (Fig. 10b, c). Exhumation of the eclogite was associated with partial melting of a large part of the Lower Unit in the Léon in a dome structure, documented to have started shortly after ca. 340 Ma (e.g., Marcoux et al., 2009; Faure et al., 2010; Authemayou et al., 2019) and to have proceeded at ca. 320 Ma with the formation of extensive and dextral ductile shearing with magmatic intrusion filling at the core of the dome.

The Léon Domain records alternating extension and compression within a back-arc domain and as such can represent a Variscan analogue to the evolution of the Central Neotethys domain (Stampfli et al., 2002; Loury et al., 2018; Alexander et al., 2019). In a recent model, Boutoux et al. (2021) interpret short-lived (15–20 Myr) alternating pulses of extension and compression as the surface expression of episodes of trench retreats and advances, ultimately linked to penetration and slab folding into the mantle transition zone. In the Neotethyan margin, a first phase of slab flattening due to penetration into the Mantle Transition Zone caused the opening of the Nain-Baft back-arc domain contemporaneously with the obduction processes recorded in Iran (Boutoux et al., 2021). Translated into the Rheic subduction system, a rifting phase in the Léon Domain causing bimodal magmatism, concomitant with the inversion and obduction of Lizard Complex, is consistent with a rollback of the Rheic trench from ca. 390 Ma (Fig. 10c). A subsequent inversion of the Léon rift domain is required less than 40 Ma later to bury the back-arc crust to depths exceeding 80 km. In the Neotethys model (Boutoux et al., 2021), this corresponds to a strong frontward motion of the slab, due to its folding within the Mantle Transition Zone and associated with very high convergence velocity and requiring 1800–2400 km of subducted lithosphere – a length that is highly plausible for the main Rheic subduction slab. Inversion could also be caused by verticalization or "chocking" of the subduction due to the subduction of a microcontinental domain south of the Lizard Complex (Brun and Faccenna, 2008; Tirel et al., 2013), or local obliquity in plate boundaries (Philippon and Corti, 2016), that could here correspond to the Rhenohercynian arc (Schulmann et al., 2022).

The intense burial of the Léon Domain requires, beyond an efficient slab pull, a strong localization of the deformation that could be facilitated by the former detachment formed during the rifting phase and a sinistral transpressional component during the beginning of the collisional stage (Faure et al., 2010; Le Gall et al., 2014). The formation of the Léon eclogites marks the last HP event associated with the subduction recorded in this part of the Rheic Ocean and could mark the completion of the oceanic subduction (Fig. 10). The exhumation of eclogites through synchronous migmatization and generation of granitic magmatism could mark yet another switch in the tectonic regime controlled by slab dynamics or rotation of plates direction (Edel et al., 2018). This exhumation is associated with the formation of strike-slip faults-bounded by volcano-sedimentary basins west and east of the Léon Domain (Ouessant southern basin, Morlaix basin; Caroff et al., 2016, 2020; Authemayou et al., 2019). The formation of these basins along with the dome exhumation is interpreted in the frame of wrenching tectonics and therefore compatible with both transpressive and pull-apart systems associated with high-T anomalies (Rolland et al., 2001; Caroff et al., 2016; Authemayou et al., 2019). The partial melting of the crust forming migmatites is linked with high thermal conditions consistently recorded in the Léon Domain (Kehornou: 325 ± 5 Ma; Faure et al., 2010; Plouguerneau: 330 ± 9 and 332 ± 5 Ma; Marcoux et al., 2009; Treglonou 334 ± 6 Ma; Faure et al., 2010) and waning at 322 ± 3 Ma, contemporaneous with SW-trending extensional shearing in the core and the southwestern border of the dome (this study; Le Gall et al., 2014; Authemayou et al., 2019). Mafic magmatism is documented just south of the Léon Domain between 347–300 Ma and shortly after. Additionally, lamprophyres dikes (kersantites), originating from partial melting of metasomatized mantle by continental crust-released fluids, have been dated ca. 330 to 310 Ma (Caroff et al., 2021). Altogether, these events require the presence of a metasomatised mantle and asthenospheric heat under the Léon Domain, and its surrounding area was located at a higher level than expected in a normal continental setting. Mantle-induced advective heat and magmatism appear to have lasted for at least 100 Ma below the Léon Domain, starting with the formation of the eclogite protolith at ca. 385 Ma and ending at or after ca. 300 Ma. Slab rollback associated with mantle delamination or slab break-off may explain this history, as well as the mafic magmatism and crustal partial melting associated with Léon dome exhumation (Rolland et al., 2001; Brun and Faccenna, 2008; Magni et al., 2013; Caroff et al., 2021; Van Hinsbergen and Schouten, 2021). The new interpretations of the Léon history, obtained here though multi-method petrochronology, support a strong control of the slab dynamics and mantle-

related heating in the frame of the protracted subduction history of the main Rheic oceanic system.

6 Conclusion

Eclogites of the Léon Domain, Armorican Massif, Variscan Orogen, were subjected to a multi-method analytical approach that integrates thermobarometric analysis using pseudosection and Zr-in-rutile thermometry, with garnet microanalysis and Lu-Hf dating, and zircon petrochronology. The results show that the protolith of these rocks represents a ca. 385 Ma igneous complex. Eclogite-facies metamorphism and HP garnet growth, which occurred at ca. 2.5 GPa and 760 °C, is dated at ca. 348 Ma. This deep burial of the Lower Unit in the Léon Domain was shortly followed with their exhumation within a migmatitic dome and triggered by a local high-thermal anomaly. Our results show that this syn-extensional, anatectic stage operated until at least ca. 322 Ma. The age for eclogite-facies metamorphism of the Léon eclogite is significantly younger, and the peak P–T conditions are higher than previous estimates for these rocks, providing substance for a shift in paradigm regarding the significance and tectonic meaning of these rocks. A model is presented in which the Léon Complex represents a back-arc context, producing both felsic and mafic intrusions (Plounévez-Lochrist orthogneiss and the eclogites protolith, respectively) emplaced contemporaneously at ca. 385 Ma close to the surface or to meteoric fluid pathways. Deep subduction of the Léon Domain records basin inversion and eventual closure. We propose that this process results from the relative motion of the slab associated with a major subduction (i.e., the Rheic Ocean) situated at the northern boundary of the Armorica microcontinent, in a scenario analogous to the Central Neotethyan system.

Data availability. All data are provided in the Supplement to this article.

Supplement. The supplement related to this article is available online at https://doi.org/10.5194/ejm-37-639-2025-supplement.

Author contributions. LT: conceptualization, funding acquisition, formal analysis, investigation, original draft writing; CA: investigation, review & editing; CL: investigation, resources, formal analysis, validation, review and editing; MAS: investigation, resources, formal analysis, review & editing; KM: investigation, review & editing; DBG: investigation, formal analysis, review & editing; EK: resources, review & editing; EB: resources, review & editing.

Competing interests. The contact author has declared that none of the authors has any competing interests.

Disclaimer. Publisher's note: Copernicus Publications remains neutral with regard to jurisdictional claims made in the text, published maps, institutional affiliations, or any other geographical representation in this paper. While Copernicus Publications makes every effort to include appropriate place names, the final responsibility lies with the authors.

Acknowledgements. Kathy Gordon (MC-ICPMS, UBC), Jessica Langlade (EPMA, Geo-Ocean), Nicolas Gayet (SEM, Ifremer), Etienne Deloule and Nordine Bouden (CRPG, LG-SIMS Nancy), and Louise Fabien and Tifenn Gourlay (BSc. students, Geo-Ocean) are warmly thanked for their technical assistance and discussions. We also thank Jean-Pierre Oldra (Geo-Ocean) for high-quality and custom-made thin sections and Chris Mark for his assistance during analytical work as part of Synthesys+ at the Swedish Museum of Natural History. Lorraine Tual and Christine Authemayou are grateful to Julien Collot and Martin Patriat (Geo-Ocean) for interesting discussions. We thank Elisabetta Rampone and Dewashish Upadhyay (Editors) as well as Yann Rolland, Paola Manzotti and the anonymous reviewer for their feedback that helped to clarify the manuscript. Fieldwork in eroded orogens is challenging; few eclogite outcrops are reported in the Léon, and we are indebted to Maurice for kindly opening his property to us and letting us sample these exceptional eclogites. This is Vegacenter publication #088.

Financial support. Funding was provided by the European Union's Horizon 2020 research and innovation program via both Marie Skłodowska-Curie (grant no. 899546 to Lorraine Tual, grant no. 896746 to Caroline Lotout) and Synthesys+ (SE-TAF, TransNational Access grant no. 823827 to Lorraine Tual) as well as Geo-Ocean (UMR6538) supporting funds to Lorraine Tual, the Natural Sciences and Engineering Research Council of Canada (Discovery Grant RGPIN-2020-04692 and Accelerator Grant RGPAS-2020-00069), the Canadian Foundation of Innovation, and the British Columbia Knowledge Development Fund (joint infrastructure grant no. 229814) to Matthijs A. Smit. NordSIMS-Vegacenter is funded by the Swedish Research Council as a national research infrastructure (#2017-00671).

Review statement. This paper was edited by Dewashish Upadhyay and reviewed by Yann Rolland, Paola Manzotti, and one anonymous referee.

References

Agard, P., Yamato, P., Jolivet, L., and Burov, E.: Exhumation of oceanic blueschists and eclogites in subduction zones: timing and mechanisms, Earth-Sci. Rev., 92, 53–79, 2009.

Angiboust, S., Pettke, T., De Hoog, J. C. M., Caron, B., and Oncken, O.: Channelized fluid flow and eclogite-facies metasomatism along the subduction shear zone, J. Pet., 55, 883–916, 2014.

Alexander, A. C., Shail, R. K., and Leveridge, B. E.: Late Paleozoic extensional reactivation of the Rheic–Rhenohercynian suture zone in SW England, the English Channel and Western Approaches, GSL Spec. Pub., 470, 353–373, 2019.

Arthaud, F. and Matte, P.: Late Paleozoic strike-slip faulting in southern Europe and northern Africa: Result of a right-lateral shear zone between the Appalachians and the Urals, GSA Bull., 88, 1305–1320, 1977.

Authemayou, C., Le Gall, B., Caroff, M., and Bussien Grosjean, D.: Wrench-related dome formation and subsequent orogenic syntax bending in a hot orogen (Variscan Ibero-Armorican Arc, the Ouessant Island, France), Tectonics, 38, 3563–3585, 2019.

Balé, P. and Brun, J. P.: Les complexes métamorphiques du Léon (NW Bretagne); un segment du domaine éo-hercynien sud armoricain translaté au Dévonien, Bulletin de la Société Géologique de France, 2, 471–477, 1986.

Ballèvre, M., Bosse, V., Ducassou, C., and Pitra, P.: Palaeozoic history of the Armorican Massif: models for the tectonic evolution of the suture zones, Comptes rendus géoscience, 341, 174–201, 2009.

Ballèvre, M., Martínez Catalán, J. R., López-Carmona, A., Pitra, P., Abati, J., Fernández, R. D., Ducassou, C., Arenas, R., Bosse, V., Castiñeiras, P., Fernández-Suárez, J., Gómez Barreiro, J., Paquette, J. L., Peucat, J. J., Poujol, M., Ruffet, G., and Sánchez Martínez, S.: Correlation of the nappe stack in the Ibero-Armorican arc across the Bay of Biscay: a joint French–Spanish project, GSL Spec. Pub., 405, 77–113, 2014.

Barnicoat, A. C. and Cartwright, I.: The gabbro–eclogite transformation: an oxygen isotope and petrographic study of west Alpine ophiolites, J. Metamorph. Geol., 15, 93–104, 1997.

Baxter, E. F. and Scherer, E. E. Garnet geochronology: timekeeper of tectonometamorphic processes, Elements, 9, 433–438, 2013.

Bebout, G. E. and Barton, M. D.: Fluid flow and metasomatism in a subduction zone hydrothermal system: Catalina Schist terrane, California, Geology, 17, 976–980, 1989.

Beckman, V., Möller, C., Söderlund, U., Corfu, F., Pallon, J., and Chamberlain, K. R.: Metamorphic zircon formation at the transition from gabbro to eclogite in Trollheimen–Surnadalen, Norwegian Caledonides, GSL Spec. Pub., 390, 403–424, 2014.

Bindeman, I.: Oxygen isotopes in mantle and crustal magmas as revealed by single crystal analysis, Rev. Mineral. Geochem., 69, 445–478, 2008.

Bizzarro, M., Baker, J. A., and Ulfbeck, D.: A new digestion and chemical separation technique for rapid and highly reproducible determination of Lu/Hf and Hf isotope ratios in geological materials by MC-ICP-MS, Geostandards Newsletter, 27, 133–145, 2003.

Blichert-Toft, J. and Albarède, F.: The Lu-Hf isotope geochemistry of chondrites and the evolution of the mantle-crust system, Earth Planet. Sc. Lett., 148, 243–258, 1997.

Blichert-Toft, J., Boyet, M., Télouk, P., and Albarède, F.: 147Sm–143Nd and 176Lu–176Hf in eucrites and the differentiation of the HED parent body, Earth Planet. Sc. Lett., 204, 167–181, 2002.

Boschetti, L., Schwartz, S., Rolland, Y., Dumont, T., and Nouibat, A.: A new tomographic-petrological model for the Ligurian-Provence back-arc basin (North-Western Mediterranean Sea), Tectonophysics, 868, 230111, https://doi.org/10.1016/j.tecto.2023.230111, 2023.

Boutoux, A., Briaud, A., Faccenna, C., Ballato, P., Rossetti, F., and Blanc, E.: Slab folding and surface deformation of the Iran mobile belt, Tectonics, 40, e2020TC006300, https://doi.org/10.1029/2020TC006300, 2021.

Bovay, T., Rubatto, D., and Lanari, P.: Pervasive fluid-rock interaction in subducted oceanic crust revealed by oxygen isotope zoning in garnet, Contrib. Mineral. Petr., 176, 1–22, 2021.

Brun, J. P. and Faccenna, C.: Exhumation of high-pressure rocks driven by slab rollback, Earth Planet. Sc. Lett., 272, 1–7, 2008.

Burg, J. P., Van Den Driessche, J., and Brun, J. P.: Syn- to post-thickening extension: Mode and structural consequences, C. R. Acad. Sci. Paris, 319, 1019–1032, 1994.

Cabanis, B., Michot, J., and Deutsch, S.: Remise en question de la datation géochronologique des gneiss de Brest (Bretagne occidentale), C. R. Acad. Sci. Paris, 284, 883–886, 1977.

Cabanis, B., Peucat, J. J., Michot, J., and Deutsch, S.: Remise en cause de l'existence d'un socle orthogneissique antécambrien dans le pays de Léon (Domaine nord-armoricain); Etude géochronologique par les méthodes Rb/Sr et U/Pb des orthogneiss de Tréglonou et de Plounevez-Lochrist, Bull. du BRGM, 4, 357–364, 1979.

Cabanis, B. and Godard, G.: Les eclogites du pays de Léon (Nord-Ouest du Massif armoricain); etude petrologique et geochimique; implications geodynamiques, Bull. de la Soc. Géol. de France, 3, 1133–1142, 1987

Caroff, M., Labry, C., Le Gall, B., Authemayou, C., Grosjean, D. B., and Guillong, M.: Petrogenesis of late-Variscan high-K alkali-calcic granitoids and calc-alkalic lamprophyres: The Aber-Ildut/North-Ouessant complex, Armorican Massif, France, Lithos, 238, 140–155, 2015.

Caroff, M., Le Gall, B., Authemayou, C., Bussien Grosjean, D., Labry, C., and Guillong, M.: Relations between basalts and adakitic–felsic intrusive bodies in a soft-substrate environment: the South Ouessant Visean basin in the Variscan belt, Armorican Massif, France, Can. J. Earth Sci., 53, 441–456, 2016.

Caroff, M., Le Gall, B., and Authemayou, C.: How does a monzogranite turn into a trachydacitic extrusion mantled by basinal volcaniclastics and peperites? The case of South-Ouessant, Armorican Variscides (France), JGS, 177, 1161–1167, 2020.

Caroff, M., Barrat, J. A., and Le Gall, B.: Kersantites and associated intrusives from the type locality (Kersanton), Variscan Belt of Western Armorica (France), Gondwana Res., 98, 46–62, 2021.

Chantraine, J., Chauris, L., Cabanis, B., Chauris, M.-M., Larsonneur, C., Herrouin, Y., C., Herrouin, Y., Rabu, D., Lulzac, Y., and Bos, P. : Notice explicative de la feuille Plestinles-Grèves à 1/50 000, Éd. Bureau Recherche Géologique et Minière, Orléans, 64 pp., 1986.

Coleman, R. G., Lee, D. E., Beatty, L. B., and Brannock, W. W.: Eclogites and eclogites: their differences and similarities, GSA Bull., 76, 483–508, 1965.

Cook, C. A., Holdsworth, R. E., and Styles, M. T.: The emplacement of peridotites and associated oceanic rocks from the Lizard Complex, southwest England, Geol. Mag., 139, 27–45, 2002.

Cruciani, G., Fancello, D., Franceschelli, M., and Rubatto, D.: Continuous vs. discontinuous garnet growth in mylonitic micaschists from northeastern Sardinia, Italy: Evidence from LA-ICPMS trace element mapping, Lithos, 464, 107436, https://doi.org//10.1016/j.lithos.2023.107436, 2024.

Cutts, J. A. and Smit, M. A.: Rates of deep continental burial from Lu-Hf garnet chronology and Zr-in-rutile thermometry on (ultra) high-pressure rocks, Tectonics, 37, 71–88, https://doi.org/10.1002/2017TC004723, 2018.

Cutts, J. A., Smit, M. A., Spengler, D., Kooijman, E., and van Roermund, H. L.: Two billion years of mantle evolution in sync with global tectonic cycles, Earth Planet. Sc. Lett., 528, 115820, https://doi.org/10.1016/j.epsl.2019.115820, 2019.

de Capitani, C. and Brown, T. H.: The computation of chemical equilibrium in complex systems containing non-ideal solutions, Geochim. Cosmochim. Ac., 51, 2639–2652, 1987.

de Capitani, C. and Petrakakis, K.: The computation of equilibrium assemblage diagrams with Theriak/Domino software, Am. Min., 95, 1006–1016, 2010.

Deloule, E., Alexandrov, P., Cheilletz, A., Laumonier, B., and Barbey, P.: In-situ U–Pb zircon ages for Early Ordovician magmatism in the eastern Pyrenees, France: the Canigou orthogneisses, IJES, 91, 398–405, 2002.

Dragovic, B., Baxter, E. F., and Caddick, M. J.: Pulsed dehydration and garnet growth during subduction revealed by zoned garnet geochronology and thermodynamic modeling, Sifnos, Greece, Earth Planet. Sc. Lett., 413, 111–122, https://doi.org/10.1016/j.epsl.2014.12.024, 2015.

Duchêne, S., Blichert-Toft, J., Luais, B., Télouk, P., Lardeaux, J. M., and Albarede, F.: The Lu–Hf dating of garnets and the ages of the Alpine high-pressure metamorphism, Nature, 387, 586–589, 1997.

Edel, J. B., Schulmann, K., Lexa, O., and Lardeaux, J. M.: Late Palaeozoic palaeomagnetic and tectonic constraints for amalgamation of Pangea supercontinent in the European Variscan belt, Earth-Sci. Rev., 177, 589–612, 2018.

Engi, M.: Petrochronology based on REE-minerals: monazite, allanite, xenotime, apatite, Rev. Mineral. Geochem., 83, 365–418, 2017.

Faure, M., Mézème, E. B., Duguet, M., Cartier, C., and Talbot, J. Y.: Paleozoic tectonic evolution of medio-Europa from the example of the French Massif Central and Massif Armoricain, Journal of the virtual Explorer, 19, 1–25, 2005

Faure, M., Sommers, C., Melleton, J., Cocherie, A., and Lautout, O.: The Léon domain (French Massif Armoricain): a westward extension of the Mid-German Crystalline rise? Structural and geochronological insights, IJES, 99, 65–81, 2010.

Floyd, P. A.: Geochemical characteristics and comparison of the basic rocks of the Lizard Complex and the basaltic lavas within the Hercynian troughs of SW England, JGS, 141, 61–70, 1984

Franke, W.: Topography of the Variscan orogen in Europe: failed–not collapsed, IJES, 103, 1471–1499, 2014.

Franke, W., Cocks, L. R. M., and Torsvik, T. H.: The palaeozoic variscan oceans revisited, Gondwana Res., 48, 257–284, 2017.

Franke, W., Ballèvre, M., Cocks, L. R. M., Torsvik, T. H., and Żelaźniewicz, A.: Variscan orogeny, in: Encyclopedia of Geology, 2nd edn., edited by: Alderton, D. and Elias, S. A., Elsevier, 338–349, https://doi.org/10.1016/B978-0-08-102908-4.00022-9, 2021.

Gapais, D. and Le Corre, C.: Is the Hercynien belt of Brittany a major shear zone?, Nature, 288, 574–576, 1980.

Gapais, D., Brun, J. P., Gumiaux, C., Cagnard, F., Ruffet, G., and Le Carlier De Veslud, C.: Extensional tectonics in the Hercynian Armorican belt (France). An overview, BSGF, 186, 117–129, 2015.

George, F. R., Gaidies, F., and Boucher, B.: Population-wide garnet growth zoning revealed by LA-ICP-MS mapping: implications for trace element equilibration and syn-kinematic deformation during crystallization, Contrib. Mineral. Petr., 173, 1–22, 2018.

George, F. R., Viete, D. R., Ávila, J., Seward, G. G., Guice, G. L., Allen, M. B., and Harrower, M. J.: Garnet zoning patterns record multiple processes of chemical transfer during subduction, Earth Planet. Sc. Lett., 631, 118634, https://doi.org/10.1016/j.epsl.2024.118634, 2024.

Gilotti, J. A.: The realm of ultrahigh-pressure metamorphism, Elements, 9, 255–260, 2013.

Godard, G.: Eclogites and their geodynamic interpretation: a history, J. Geodyn., 32, 165–203, 2001.

Godard, G. and Mabit, J. L.: Peraluminous sapphirine formed during retrogression of a kyanite-bearing eclogite from Pays de Léon, Armorican Massif, France, Lithos, 43, 15–29, 1998.

Green, E. C. R., White, R. W., Diener, J. F. A., Powell, R., Holland, T. J. B., and Palin, R. M.: Activity–composition relations for the calculation of partial melting equilibria in metabasic rocks, J. Metamorph. Geol., 34, 845–869, 2016.

Griffin, W. L. and Brueckner, H. K.: Caledonian Sm–Nd ages and a crustal origin for Norwegian eclogites, Nature, 285, 319–321, 1980.

Guffroy, J.: Sur quelques gisements d'amphibolites et de pyroxénites du Finistère (feuille Plouguernau à 1/80 000), Bull. Serv. Carte géol. Fr, 238, 1–7, ISBN 2-7159-1238-2, 1958.

Guiraud, M., Powell, R., and Rebay, G.: H_2O in metamorphism and unexpected behaviour in the preservation of metamorphic mineral assemblages, J. Metamorph. Geol., 19, 445–454, 2001.

Gutiérrez-Alonso, G., Johnston, S. T., Weil, A. B., Pastor-Galán, D., and Fernández-Suárez, J.: Buckling an orogen: The Cantabrian Orocline, GSA Today, 22, 4–9, 2012.

He, H. L., Song, X. Y., Zhai, M. G., Yu, S. Y., and Du, Z. S.: Lower crustal contribution to the magma formation of the Damiao massif-type anorthosite, North China Craton: Evidence from zircon Hf-O isotopes, Precamb. Res., 332, 105396, https://doi.org/10.1016/j.precamres.2019.105396, 2019.

Holland, T. J. B.: AX62 activity-composition program for minerals, University of Cambridge, Cambridge, https://filedn.com/lU1GlyFhv3UuXg5E9dbnWFF/TJBHpages/ax.html (last access: 19 November 2024), 2018.

Holland, T. J. B. and Powell, R.: An improved and extended internally consistent thermodynamic dataset for phases of petrological interest, involving a new equation of state for solids, J. Metamorph. Geol., 29, 333–383, 2011.

Holland, T. J. B., Green, E. C. R., and Powell, R.: A thermodynamic model for feldspars in $KAlSi_3O_8^-$ $NaAlSi_3O_8^-$ $CaAl_2Si_2O_8$ for mineral equilibrium calculations, J. Metamorph. Geol., 40, 587–600, 2022.

Jackson, S. E.: LAMTRACE data reduction software for LA-ICP-MS, in: Laser ablation ICP-MS in the Earth sciences: Current practices and outstanding issues, edited by: Sylvester, P., Mineralogical Association of Canada Short Course Series, 40, 305–307, 2008.

Jackson, S. E., Pearson, N. J., Griffin, W. L., and Belousova, E. A.: The application of laser ablation-inductively coupled plasma-mass spectrometry to in situ U–Pb zircon geochronology, Chem. Geol., 211, 47–69, 2004.

Jeon, H. and Whitehouse, M. J.: A critical evaluation of U–Pb calibration schemes used in SIMS zircon geochronology, Geostand. Geoanal. Res., 39, 443–452, 2015.

Johnson, M. R. and Harley, S. L.: Orogenesis: the making of mountains, Cambridge University Press, New York, 110, 388 pp., ISBN 978-0-521-76556-5, 2012.

Jones, K. A.: Phase relations in Al2SiO5 polymorphs; Le Conquet region, North-Western Brittany, France, Proceedings of the Ussher Society, 8, 138–144, 1993.

Jones, K. A.: Progressive metamorphism in a crustal-scale shear zone: An example from the Léon region, north-west Brittany, France, J. Metamorph. Geol., 12, 69–88, 1994.

Kohn, M. J.: Himalayan metamorphism and its tectonic implications, Annu. Rev. Earth Planet. Sci., 42, 381–419, 2014.

Kohn, M. J., Corrie, S. L., and Markley, C.: The fall and rise of metamorphic zircon, Am. Min., 100, 897–908, 2015.

Kooijman, E., Smit, M. A., Ratschbacher, L., and Kylander-Clark, A. R.: A view into crustal evolution at mantle depths, Earth Planet. Sc. Lett., 465, 59–69, 2017.

Konrad-Schmolke, M., Halama, R., Chew, D., Heuzé, C., De Hoog, J., and Ditterova, H.: Discrimination of thermodynamic and kinetic contributions to the heavy rare earth element patterns in metamorphic garnet, J. Metamorph. Geol., 41, 465–490, 2023.

Kroner, U. and Romer, R. L.: Two plates–many subduction zones: the Variscan orogeny reconsidered, Gond. Res., 24, 298–329, 2013.

Kulhánek, J. and Faryad, S. W.: Compositional changes in garnet: trace element transfer during eclogite-facies metamorphism, Contrib. Mineral. Petr., 178, 68, https://doi.org/10.1007/s00410-023-02050-8, 2023.

Kylander-Clark, A. R., Hacker, B. R., Johnson, C. M., Beard, B. L., Mahlen, N. J., and Lapen, T. J.: Coupled Lu–Hf and Sm–Nd geochronology constrains prograde and exhumation histories of high-and ultrahigh-pressure eclogites from western Norway, Chem. Geol., 242, 137–154, 2007.

Kylander-Clark, A. R. C., Hacker, B. R., and Mattinson, C.: Size and exhumation rate of ultrahigh-pressure terranes linked to orogenic stage, Earth Planet. Sc. Lett., 321, 115–120, https://doi.org/10.1016/j.epsl.2011.12.036, 2012.

Lacroix, A.: Contribution à l'étude des gneiss à pyroxène et des roches à wernérite, BSGF, 12, 83–360, 1889.

Lacroix, A.: Etude pétrogrpahique des éclogites de la Loire inférieure, BSGF, 7, 1191–1205, 1891.

Lagos, M., Scherer, E. E., Tomaschek, F., Münker, C., Keiter, M., Berndt, J., and Ballhaus, C.: High precision Lu–Hf geochronology of Eocene eclogite-facies rocks from Syros, Cyclades, Greece, Chem. Geol., 243, 16–35, 2007.

Lanari, P. and Engi, M.: Local bulk composition effects on metamorphic mineral assemblages, Rev. Mineral. Geochem., 83, 55–102, 2017.

Lanari, P., Vidal, O., De Andrade, V., Dubacq, B., Lewin, E., Grosch, E. G., and Schwartz, S.: XMapTools: A MATLAB©-based program for electron microprobe X-ray image processing and geothermobarometry, Comput. Geosci., 62, 227–240, 2014.

Lanari, P., Vho, A., Bovay, T., Airaghi, L., and Centrella, S.: Quantitative compositional mapping of mineral phases by electron probe micro-analyser, GSL Spec. Pub., 478, 39–63, 2019.

Leake, B. E., Woolley, A. R., Birch, W. D., Burke, E. A., Ferraris, G., Grice, J. D., Hawthorne, F. C., Kisch, H. J., Krivovichev, V. G., Schumacher, J. C., Stephenson, N. C. N., and Whittaker, E. J.: Nomenclature of amphiboles: additions and revisions to the International Mineralogical Association's amphibole nomenclature, Mineral. Mag., 68, 209–215, 2004.

Le Corre, C., Bale, P., and Georget, Y.: Le Léon: un domaine exotique au Nord-Ouest de la chaine varisque armoricaine (France), Geo. Acta, 3, 57–71, 1989.

Le Corre, C., Auvray, B., Ballèvre, M., and Robardet, M.: Le Massif Armoricain/The Armorican Massif, Sciences Géologiques, bulletins et mémoires, 44, 31–103, 1991.

Le Gall, B., Authemayou, C., Ehrhold, A., Paquette, J. L., Bussien, D., Chazot, G., Aouizerat, A., and Pastol, Y.: LiDAR offshore structural mapping and U/Pb zircon/monazite dating of Variscan strain in the Léon metamorphic domain, NW Brittany, Tectonophysics, 630, 236–250, https://doi.org/10.1016/j.tecto.2014.05.026, 2014.

Leveridge, B. E. and Shail, R. K.: The Gramscatho basin, south Cornwall, UK: Devonian active margin successions, Proceedings of the Geologists' Association, 122, 568–615, 2011.

Lotout, C., Pitra, P., Poujol, M., Anczkiewicz, R., and Van Den Driessche, J.: Timing and duration of Variscan high-pressure metamorphism in the French Massif Central: A multimethod geochronological study from the Najac Massif, Lithos, 308, 381–394, 2018.

Lotout, C., Poujol, M., Pitra, P., Anczkiewicz, R., and Van Den Driessche, J.: From burial to exhumation: emplacement and metamorphism of mafic eclogitic terranes constrained through multimethod petrochronology, case study from the Lévézou Massif (French Massif Central, Variscan Belt), J. Petrol., 61, egaa046, https://doi.org/10.1093/petrology/egaa046, 2020.

Lotout, C., Indares, A., Vervoort, J., and Deloule, E.: High-P metamorphism in the Mesoproterozoic: petrochronological insights from the Grenville Province, Precamb. Res., 399, 107208, https://doi.org/10.1016/j.precamres.2023.107208, 2023.

Loury, C., Rolland, Y., Guillot, S., Lanari, P., Ganino, C., Melis, R., Jourdon, A., Petit, C., Beyssac, O., Gallet, S., and Monié, P.: Tectonometamorphic evolution of the Atbashi high-P units (Kyrgyz CAOB, Tien Shan): Implications for the closure of the Turkestan Ocean and continental subduction–exhumation of the South Kazakh continental margin, J. Metamorph. Geol., 36, 959–985, 2018.

Ludwig, K. R.: User's manual for IsoPlot 3.0. A geochronological toolkit for Microsoft Excel, Berkeley Geochronology Center, Berkeley, Special Publication, 4, 1–70, 2003.

Ludwig, K. R.: User's manual for Isoplot 3.75: A geochronological toolkit for Microsoft Excel, Berkeley Geochronology Center Special Publication, 5, 1–75, 2012.

Magni, V., Faccenna, C., van Hunen, J., and Funiciello, F.: Delamination vs. break-off: The fate of continental collision, Geophys. Res. Lett., 40, 285–289, 2013.

Marcoux, E., Cocherie, A., Ruffet, G., Darboux, J. R., and Guerrot, C.: Géochronologie revisitée du dôme du Léon (Massif armoricain, France), Géol. de la France, 1, 19–40, 2009.

Martin, L., Duchêne, S., Deloule, E., and Vanderhaeghe, O.: The isotopic composition of zircon and garnet: A record of the metamorphic history of Naxos, Greece, Lithos, 87, 174–192, 2006.

Martínez Catalán, J. R.: Are the oroclines of the Variscan belt related to late Variscan strike-slip tectonics?, Terra Nova, 23, 241–247, 2011.

Martínez Catalán, J. R., Schulmann, K., Ayarza, P., Edel, J. B., and Durán Oreja, M.: Oroclinal arcs of the Variscan Belt: a conse-

quence of transpression during the consolidation of Pangaea, J. Geol. Soc., 181, jgs2024-007, https://doi.org/10.1144/jgs2024-007, 2024.

Maruyama, S., Liou, J. G., and Terabayashi, M.: Blueschists and eclogites of the world and their exhumation, Int. Geol. Rev., 38, 485–594, 1996.

Mateus, A., Munhá, J., Ribeiro, A., Tassinari, C. C. G., Sato, K., Pereira, E., and Santos, J. F.: U–Pb SHRIMP zircon dating of high-grade rocks from the Upper Allochthonous Terrane of Bragança and Morais Massifs (NE Portugal); geodynamic consequences, Tectonophysics, 675, 23–49, 2016.

Matte, P.: La chaîne varisque parmi les chaînes paléozoïques péri atlantiques, modèle d'évolution et position des grands blocs continentaux au Permo-Carbonifère, BSGF, 2, 9–24, 1986.

Matte, P.: The Variscan collage and orogeny (480–290 Ma) and the tectonic definition of the Armorica microplate: a review, Terra Nova, 13, 122–128, 2001.

Matte, P. and Ribeiro, A.: Forme et orientation de l'ellipsoide de déformation dans la virgation hercynienne de Galice. Relation avec le plissement et hypothèse sur la genèse de l'arc ibéro-armoricain, Comptes Rendus de l'Académie des Sciences, Paris, 280, 2825–2828, 1975.

McDonough, W. F. and Sun, S. S.: The composition of the Earth, Chem. Geol., 120, 223–253, 1995.

Moreira, N., Romão, J., Dias, R., Ribeiro, A., and Pedro, J.: The Finisterra-Léon-Mid German Cristalline Rise Domain; Proposal of a New Terrane, in: The Variscan Chain. The Geology of Iberia: A Geodynamic Approach: Volume 2: The Variscan Cycle, edited by: Quesada, C. and Oliveira, J., Regional Geology Reviews, Springer, Cham, 207–228, https://doi.org/10.1007/978-3-030-10519-8_7, 2019.

Morimoto, N.: Nomenclature of Pyroxenes, Miner. Petrol., 39, 55–76, https://doi.org/10.1007/BF01226262, 1988.

Münker, C., Weyer, S., Scherer, E., and Mezger, K.: Separation of high field strength elements (Nb, Ta, Zr, Hf) and Lu from rock samples for MC-ICPMS measurements, G^3, 2, 12, 1064, 2001.

Murphy, J. B., Nance, R. D., and Cawood, P. A.: Contrasting modes of supercontinent formation and the conundrum of Pangea, Gondwana Res., 15, 408–420, 2009.

Nutman, A. P., Bennett, V. C., Green, D. H., and Friend, C. R.: Evolution of the Palaeozoic mafic-ultramafic Lizard Complex (SW England) from zircon and baddeleyite U-Pb-Hf isotopic constraints: New thoughts on the convergence of Avalonia and Armorica, Lithos, 452, 107227, https://doi.org/10.1016/j.lithos.2023.107227, 2023.

Paquette, J. L., Balé, P., Ballèvre, M., and Georget, Y.: Géochronologie et géochimie des éclogites du Léon: nouvelles contraintes sur l'évolution géodynamique du Nord-Ouest du Massif Armoricain, Bulletin de Minéralogie, 110, 683–696, 1987.

Paquette, J. L., Monchoux, P., and Couturier, M.: Geochemical and isotopic study of a norite-eclogite transition in the European Variscan belt: Implications for U Pb zircon systematics in metabasic rocks, Geochim. Cosmochim. Ac., 59, 1611–1622, 1995.

Paquette, J. L., Ballèvre, M., Peucat, J. J., and Cornen, G.: From opening to subduction of an oceanic domain constrained by LA-ICP-MS U-Pb zircon dating (Variscan belt, Southern Armorican Massif, France), Lithos, 294, 418–437, 2017.

Pastor-Galán, D., Groenewegen, T., Brouwer, D., Krijgsman, W., and Dekkers, M. J.: One or two oroclines in the Variscan orogen of Iberia? Implications for Pangea amalgamation, Geology, 43, 527–530, 2015.

Paton, C., Hellstrom, J., Paul, B.,Woodhead, J., and Hergt, J.: Iolite: Freeware for the visualisation and processing of mass spectrometric data, JAAS, 26, 12, 2508–2518, 2011.

Paul, B., Paton, C., Norris, A., Woodhead, J., Hellstrom, J., Hergt, J., and Greig, A.: CellSpace: A module for creating spatially registered laser ablation images within the Iolite freeware environment, J. Anal. Atom. Spectrom., 27, 700–706, 2012.

Paul, B., Woodhead, J. D., Paton, C., Hergt, J. M., Hellstrom, J., and Norris, C. A.: Towards a method for quantitative LA-ICP-MS imaging of multi-phase assemblages: mineral identification and analysis correction procedures, Geostand. Geoanal. Res., 38, 253–263, 2014.

Petersson, A. and Tual, L.: Zircon U–Pb-Hf isotope data in eclogite and metagabbro from southern Sweden reveal a common long-lived evolution and enriched source, GFF, 142, 253–266, https://doi.org/10.1080/11035897.2020.1822438, 2020.

Petrus, J. A., Chew, D. M., Leybourne, M. I., and Kamber, B. S.: A new approach to laser-ablation inductively-coupled-plasma mass-spectrometry (LA-ICP-MS) using the flexible map interrogation tool "Monocle", Chem. Geol., 463, 76–93, 2017.

Philippon, M. and Corti, G.: Obliquity along plate boundaries, Tectonophysics, 693, 171–182, 2016.

Pitra, P., Poujol, M., Van Den Driessche, J., Bretagne, E., Lotout, C., and Cogné, N.: Late Variscan (315 Ma) subduction or deceptive zircon REE patterns and U–Pb dates from migmatite-hosted eclogites? (Montagne Noire, France), J. Metamorph. Geol., 40, 39–65, 2022.

Pollington, A. D. and Baxter, E. F.: High resolution Sm–Nd garnet geochronology reveals the uneven pace of tectonometamorphic processes, Earth Planet. Sc. Lett., 293, 63–71, https://doi.org/10.1016/j.epsl.2010.02.019, 2010.

Powell, R. and Holland, T.: Optimal geothermometry and geobarometry, Am. Min., 79, 120–133, 1994.

Pupin, J. P.: Zircon and granite petrology, Contrib. Mineral. Petr., 73, 207–220, 1980.

Putlitz, B., Matthews, A., and Valley, J. W.: Oxygen and hydrogen isotope study of high-pressure metagabbros and metabasalts (Cyclades, Greece): implications for the subduction of oceanic crust, Contrib. Mineral. Petr., 138, 114–126, 2000.

Raimondo, T., Payne, J., Wade, B., Lanari, P., Clark, C., and Hand, M.: Trace element mapping by LA-ICP-MS: assessing geochemical mobility in garnet, Contrib. Mineral. Petr., 172, 1–22, 2017.

Reimink, J. R., Chacko, T., Stern, R. A., and Heaman, L. M.: Earth's earliest evolved crust generated in an Iceland-like setting, Nat. Geosci., 7.7, 529–533, 2014.

Ribeiro, A., Munhá, J., Mateus, A., Fonseca, P., Pereira, E., Noronha, F., Romao, J., Rodrigues, J., Castro, P., Meireles, C., and Ferreira, N.: Mechanics of thick-skinned Variscan overprinting of Cadomian basement (Iberian Variscides), Comptes Rendus Geoscience, 341, 127–139, 2009.

Rolet, J.: Introduction to structure and metamorphism in the Armorican Massif, France, in: Pre-Mesozoic geology in France and related areas, edited by: Keppie, J. D., Berlin, Heidelberg, Springer-Verlag, 177–178, 1994.

Rolet, J., Le Gall, B., Darboux, J. R., Thonon, P., and Gravelle, M.: L'évolution géodynamique dévono-carbonifère de l'extrémité occidentale de la chaîne hercynienne d'Europe sur le transect Armorique-Cornwall, BGSF, 2, 43–54, 1986.

Rolland, Y., Mahéo, G., Guillot, S., and Pêcher, A.: Tectono-metamorphic evolution of the Karakorum Metamorphic complex (Dassu–Askole area, NE Pakistan): Exhumation of mid-crustal HT–MP gneisses in a convergent context, J. Metamorph. Geol., 19, 717–737, 2001.

Rubatto, D.: Zircon trace element geochemistry: partitioning with garnet and the link between U–Pb ages and metamorphism, Chem. Geol., 184, 123–138, 2002.

Rubatto, D.: Zircon: The metamorphic mineral, Rev. Mineral. Geochem., 83, 261–295, 2017.

Rubatto, D., Burger, M., Lanari, P., Hattendorf, B., Schwarz, G., Neff, C., Keresztes Schmidt, P., Hermann, J., Vho, A., and Günther, D.: Identification of growth mechanisms in metamorphic garnet by high-resolution trace element mapping with LA-ICP-TOFMS, Contrib. Mineral. Petr., 175, 61, https://doi.org/10.1007/s00410-020-01700-5, 2020.

Scambelluri, M., Fiebig, J., Malaspina, N., Müntener, O., and Pettke, T.: Serpentinite subduction: implications for fluid processes and trace-element recycling, Int. Geol. Rev., 46, 595–613, 2004.

Scherer, E. E., Cameron, K. L., and Blichert-Toft, J.: Lu–Hf garnet geochronology: closure temperature relative to the Sm–Nd system and the effects of trace mineral inclusions, Geochim. Cosmochim. Ac., 64, 3413–3432, 2000.

Scherer, E., Munker, C., and Mezger, K.: Calibration of the lutetium-hafnium clock, Science, 293, 683–687, 2001.

Schulmann, K., Edel, J. B., Catalán, J. R. M., Mazur, S., Guy, A., Lardeaux, J. M., Ayarza, P., and Palomeras, I.: Tectonic evolution and global crustal architecture of the European Variscan belt constrained by geophysical data, Earth-Sci. Rev., 234, 104195, https://doi.org/10.1016/j.earscirev.2022.104195, 2022.

Schulmann, K., Edel, J. B., Lexa, O., Xiao, W., Třebínová, D., Spikings, Schaltegger, U., Derkowsk, A., and Szczerba, M.: Paleomagnetic, tectonic and geochronological constraints for Permian–Triassic oroclinal bending of the Mongolian collage, Natl. Sci. Rev., 10, nwac184, https://doi.org/10.1093/nsr/nwac184, 2023.

Schulz, B.: Monazite EMP-Th-U-Pb age pattern in Variscan metamorphic units in the Armorican massif (Brittany, France), Zeitschrift der Deutschen Gesellschaft für Geowissenschaften, 164, 313–335, 2013.

Schulz, B., Krenn, E., Finger, F., Brätz, H., Klemd, R., Schulz, B., Krenn, E., Finger, F., Bratz, H., and Klemd, R.: Cadomian and Variscan metamorphic events in the Léon domain (Armorican massif, France): P-T data and EMP monazite dating, in: The evolution of the Rheic Ocean from Avalonian-Cadomian active margin to Alleghenian-Variscan collision, edited by: Linneman, U., Nance, R., and Kraft, P., Special Papers, vol. 423, 267–285, Geological Society, America, 2007.

Servais, T. and Sintubin, M.: Avalonia, Armorica, Perunica: terranes, microcontinents, microplates or palaeobiogeographical provinces?, GSL Spec. Pub., 325, 103–115, 2009.

Shail, R. K. and Leveridge, B. E.: The Rhenohercynian passive margin of SW England: Development, inversion and extensional reactivation, Comptes Rendus Géoscience, 341, 140–155, 2009.

Sharp, Z. D., Essene, E. J., and Hunziker, J. C.: Stable isotope geochemistry and phase equilibria of coesite-bearing whiteschists, Dora Maira Massif, western Alps, Contrib. Mineral. Petr., 114, 1–12, 1993.

Sláma, J., Košler, J., Condon, D. J., Crowley, J. L., Gerdes, A., Hanchar, J. M., Horstwood, M. S. A., Morris, G. A., Nasdala, L., Norberg, N., Schaltegger, U., Schoene, B., Tubrett, M. N., and Whitehouse, M. J.: Plešovice zircon–a new natural reference material for U–Pb and Hf isotopic microanalysis, Chem. Geol., 249, 1–35, 2008.

Smit, M. A., Scherer, E. E., Bröcker, M., and van Roermund, H. L. M.: Timing of eclogite facies metamorphism in the southernmost Scandinavian Caledonides by Lu–Hf and Sm–Nd geochronology, Contrib. Mineral. Petr., 159, 521–539, https://doi.org/10.1007/s00410-009-0440-3, 2010.

Smit, M. A., Scherer, E. E., and Mezger, K.: Lu–Hf and Sm–Nd garnet geochronology: chronometric closure and implications for dating petrological processes, Earth Planet. Sc. Lett., 381, 222–233, 2013.

Smit, M. A., Vrijmoed, J. C., Scherer, E. E., Mezger, K., Kooijman, E., Schmitt-Kielman, M., Tual, L., Guilmette, C., and Ratschbacher, L.: Retentiveness of rare earth elements in garnet with implications for garnet Lu-Hf chronology, J. Metamorph. Geol., 42, 703–727, 2024.

Söderlund, U., Patchett, P. J., Vervoort, J. D., and Isachsen, C. E.: The ^{176}Lu decay constant determined by Lu–Hf and U–Pb isotope systematics of Precambrian mafic intrusions, Earth Planet. Sc. Lett., 219, 311–324, 2004.

Spear, F. S.: Metamorphic phase equilibria and pressure–temperature–time paths, Mineralogical Society of America Monograph, 352 pp., ISBN 0-939950-34-0, 1993.

Sprung, P., Scherer, E. E., Upadhyay, D., Leya, I., and Mezger, K.: Non-nucleosynthetic heterogeneity in non-radiogenic stable Hf isotopes: Implications for early solar system chronology, Earth Planet. Sc. Lett., 295, 1–11, 2010.

Stampfli, G. M., Raumer, J. F. V., and Borel, G. D.: Paleozoic evolution of pre-Variscan terranes: from Gondwana to the Variscan collision. Variscan-Appalachian dynamics: The building of the late Paleozoic basement, GSA Spec. Paper 364, 263–280, 2002.

Stampfli, G. M., Hochard, C., Vérard, C., and Wilhem, C.: The formation of Pangea, Tectonophysics, 593, 1–19, 2013.

Tait, J.: New Early Devonian paleomagnetic data from NW France: Paleogeography and implications for the Armorican microplate hypothesis, J. Geophys. Res.-Sol. Ea., 104, 2831–2839, 1999.

Tirel, C., Brun, J. P., Burov, E., Wortel, M. J. R., and Lebedev, S.: A plate tectonics oddity: Caterpillar-walk exhumation of subducted continental crust, Geology, 41, 555–558, 2013.

Tomkins, H. S., Powell, R., and Ellis, D. J.: The pressure dependence of the zirconium-in-rutile thermometer, J. Metamorph. Geol., 25, 703–713, 2007.

Tsujimori, T. and Mattinson, C.: Eclogites in different tectonic settings, Encyclopedia of geology, 561–568, 2021.

Tual, L., Pitra, P., and Möller, C.: P–T evolution of Precambrian eclogite in the Sveconorwegian orogen, SW Sweden, J. Metamorph. Geol., 35, 493–515, 2017.

Tual, L., Möller, C., and Whitehouse, M. J.: Tracking the prograde P–T path of Precambrian eclogite using Ti-in-quartz and Zr-in-rutile geothermobarometry, Contrib. Mineral. Petr., 173, 56, https://doi.org/10.1007/s00410-018-1482-1, 2018.

Tual, L., Smit, M. A., Cutts, J., Kooijman, E., Kielman-Schmitt, M., Majka, J., and Foulds, I.: Rapid, paced metamorphism of blueschists (Syros, Greece) from laser-based zoned Lu-Hf garnet chronology and LA-ICPMS trace element mapping, Chem. Geol., 607, 121003, https://doi.org/10.1016/j.chemgeo.2022.121003, 2022a.

Tual, L., Smit, M. A., Kooijman, E., Kielman-Schmitt, M., and Ratschbacher, L.: Garnet, zircon, and monazite age and REE signatures in (ultra) high-temperature and high-pressure rocks: Examples from the Caledonides and the Pamir, J. Metamorph. Geol., 40, 1321–1346, 2022b.

Tual, L., Smit, M. A., Cutts, J. A., Musiyachenko, K. A., Kooijman, E., Majka, J., Foulds, I., and Ielpi, A.: Garnet growth in a geological blink of an eye, Geology, 53, 248–252, https://doi.org/10.1130/G52772.1, 2025.

Ulianov, A., Müntener, O., Schaltegger, U., and Bussy, F.: The data treatment dependent variability of U–Pb zircon ages obtained using mono-collector, sector field, laser ablation ICPMS, J. Anal. Atom. Spectrom., 27, 663–676, 2012.

Valley, J. W., Kinny, P. D., Schulze, D. J., and Spicuzza, M. J.: Zircon megacrysts from kimberlite: oxygen isotope variability among mantle melts, Contrib. Mineral. Petr., 133, 1–11, 1998.

Van Hinsbergen, D. J. and Schouten, T. L.: Deciphering paleogeography from orogenic architecture: constructing orogens in a future supercontinent as thought experiment, Am. J. Sci., 321, 955–1031, 2021.

Vho, A., Rubatto, D., Putlitz, B., and Bouvier, A. S.: New reference materials and assessment of matrix effects for SIMS measurements of oxygen isotopes in garnet, Geostand. Geoanal. Res., 44, 459–471, 2020.

Walters, J. B.: MinPlot: A mineral formula recalculation and plotting program for electron probe microanalysis, Mineralogia, 53, 51–66, 2022.

Warren, C. J.: Exhumation of (ultra-)high-pressure terranes: concepts and mechanisms, Solid Earth, 4, 75–92, https://doi.org/10.5194/se-4-75-2013, 2013.

Weil, A. B., Van der Voo, R., and Van Der Pluijm, B. A.: Oroclinal bending and evidence against the Pangea megashear: The Cantabria-Asturias arc (northern Spain), Geology, 29, 991–994, 2001.

Weil, A. B., Gutiérrez-Alonso, G., Johnston, S. T., and Pastor-Galán, D.: Kinematic constraints on buckling a lithospheric-scale orocline along the northern margin of Gondwana: A geologic synthesis, Tectonophysics, 582, 25–49, 2013.

White, R. W., Powell, R., Holland, T., and Worley, B. A.: The effect of TiO_2 and Fe_2O_3 on metapelitic assemblages at greenschist and amphibolite facies conditions: mineral equilibria calculations in the system K_2O-FeO-MgO-Al_2O_3-SiO_2-H_2O-TiO_2-Fe_2O_3, J. Metamorph. Geol., 18, 497–511, 2000.

White, R. W., Powell, R., Holland, T., Johnson, T. E., and Green, E. C. R.: New mineral activity–composition relations for thermodynamic calculations in metapelitic systems. J. Metamorph. Geol., 32, 261–286, 2014a.

White, R. W., Powell, R., and Johnson, T. E.: The effect of Mn on mineral stability in metapelites revisited: New a–x relations for manganese-bearing minerals, J. Metamorph. Geol., 32, 809–828, 2014b.

Wiedenbeck, M. A. P. C., Alle, P., Corfu, F. Y., Griffin, W. L., Meier, M., Oberli, F. V., Von Quadt, A., Roddick, J. C., and Spiegel, W.: Three natural zircon standards for U-Th-Pb, Lu-Hf, trace element and REE analyses, Geostandards newsletter, 19, 1–23, 1995.

Wiedenbeck, M., Hanchar, J. M., Peck, W. H., Sylvester, P., Valley, J., Whitehouse, M., Kronz, A., Morishita, Y., Nasdala, L., Fiebig, J., Franchi, I., Girard, J. P., Greenwood, R. C., Hinton, R., Kita, N., Mason, P. R. D., Norman, M., Ogasawara, M., Piccoli, P. M., Rhede, D., Satoh, H., Schulz Dobrick, B., Skår, O., Spicuzza, M. J., Terada, K., Tindle, A., Togashi, S., Vennemann, T., Xie, Q., and Zheng, Y. F.: Further characterisation of the 91500 zircon crystal, Geostand. Geoanal. Res., 28, 9–39, 2004.

Wilbur, D. E. and Ague, J. J.: Chemical disequilibrium during garnet growth: Monte Carlo simulations of natural crystal morphologies, Geology, 34, 689–692, 2006.

Woodhead, J. D., Hellstrom, J., Hergt, J. M., Greig, A., and Maas, R.: Isotopic and elemental imaging of geological materials by Laser Ablation Inductively Coupled Plasma-Mass Spectrometry, Geostand. Geoanal. Res., 31, 331–343, 2007.

Young, T. P.: Ordovician sedimentary facies and faunas of southwest Europe: palaeogeographic and tectonic implications, Geol. Soc. London Memoirs, 12, 421–430, 1990.

Zack, T., Moraes, R. D., and Kronz, A.: Temperature dependence of Zr in rutile: empirical calibration of a rutile thermometer, Contrib. Mineral. Petr., 148, 471–488, 2004.

Zheng, Y. F.: Metamorphic chemical geodynamics in continental subduction zones, Chem. Geol., 328, 5–48, 2012.

Ziegler, P. A.: Late Cretaceous and Cenozoic intra-plate compressional deformations in the Alpine foreland – a geodynamic model, Tectonophysics, 137, 389–420, 1987.

Ziegler, P. A.: Cenozoic rift system of Western and Central-European overview, Neth. J. Geosci., 73, 99–127, 1994.